

Optical Flares from the Tidal Disruption of Stars by Massive Black Holes

Linda E. Strubbe^{1*}, Eliot Quataert¹

¹*Astronomy Department and Theoretical Astrophysics Center, 601 Campbell Hall, University of California, Berkeley CA, 94720, USA*

Accepted for publication in MNRAS

ABSTRACT

A star that wanders too close to a massive black hole (BH) is shredded by the BH’s tidal gravity. Stellar gas falls back to the BH at a rate initially exceeding the Eddington rate, releasing a flare of energy. In anticipation of upcoming transient surveys, we predict the light curves and spectra of tidal flares as a function of time, highlighting the unique signatures of tidal flares at optical and near-infrared wavelengths. A reasonable fraction of the gas initially bound to the BH is likely blown away when the fallback rate is super-Eddington at early times. This outflow produces an optical luminosity comparable to that of a supernova; such events have durations of ~ 10 days and may have been missed in supernova searches that exclude the nuclear regions of galaxies. When the fallback rate subsides below Eddington, the gas accretes onto the BH via a thin disk whose emission peaks in the UV to soft X-rays. Some of this emission is reprocessed by the unbound stellar debris, producing a spectrum of very broad emission lines (with no corresponding narrow forbidden lines). These lines are the strongest for BHs with $M_{\text{BH}} \sim 10^5 - 10^6 M_{\odot}$ and thus optical surveys are particularly sensitive to the lowest mass BHs in galactic nuclei. Calibrating our models to ROSAT and GALEX observations, we predict detection rates for Pan-STARRS, PTF, and LSST and highlight some of the observational challenges associated with studying tidal disruption events in the optical. Upcoming surveys such as Pan-STARRS should detect at least several events per year, and may detect many more if current models of outflows during super-Eddington accretion are reasonably accurate. These surveys will significantly improve our knowledge of stellar dynamics in galactic nuclei, the physics of super-Eddington accretion, the demography of intermediate mass BHs, and the role of tidal disruption in the growth of massive BHs.

Key words: galaxies: nuclei — black hole physics — optical: galaxies

1 INTRODUCTION

Stellar orbits in the center of a galaxy are not static, and sometimes stars walk into trouble. If an unlucky star passes within $R_{\text{T}} \sim R_{\star}(M_{\text{BH}}/M_{\star})^{1/3}$ of the galaxy’s central black hole (BH), the BH’s tidal gravity exceeds the star’s self-gravity, and the star is disrupted. For BHs with $M_{\text{BH}} \leq 10^8 M_{\odot}$, the disruption of a solar-type star occurs outside the horizon and is likely accompanied by a week- to year-long electromagnetic flare (e.g., Rees 1988).

Gravitational interactions between stars ensure that all supermassive BHs tidally disrupt nearby stars (e.g., Magorrian & Tremaine 1999). The scattering process might be accelerated by resonant relaxation very close to the BH (Rauch & Tremaine 1996), or interactions with “massive

perturbers” like a massive accretion disk (Zhao et al. 2002) or giant molecular clouds (Perets et al. 2007). In addition, the galactic potential may be triaxial so stars need not be scattered at all: they may simply follow their chaotic orbits down to $\sim R_{\text{T}}$ (Merritt & Poon 2004). Given these uncertainties, predictions for the timescale between tidal disruptions in a given galaxy range from 10^3 to 10^6 years. The rate remains uncertain, but tidal disruption must occur.

Indeed, a handful of candidate events have been detected to date. The accreting stellar debris is expected to emit blackbody radiation from very close to the BH, so X-ray and UV observations probe the bulk of the emission. Several candidate tidal disruption events were discovered in the ROSAT All-Sky Survey (see Komossa 2002) and the XMM-Newton Slew Survey (Esquej et al. 2007); the GALEX Deep Imaging Survey has so far yielded three candidates (Gezari et al. 2006, 2008, 2009). For ROSAT,

* E-mail: linda@astro.berkeley.edu

these detections are consistent with a rate $\sim 10^{-5} \text{ yr}^{-1}$ per galaxy (Donley et al. 2002), but the data are sparse. However, we are entering a new era of transient surveys: in the optical, surveys like Pan-STARRS (PS1, then all four telescopes) (e.g., Magnier 2007), the Palomar Transient Factory (Rau et al. 2009), and later the Large Synoptic Survey Telescope will have fast cadence, wide fields of view, and unprecedented sensitivity. Wide-field transient surveys with rapid cadence are also planned at other wavelengths, including the radio (e.g., LOFAR and the ATA), near-infrared (e.g., SASIR), and hard X-rays (e.g., EXIST). How many tidal flares these surveys find depends on their luminosity and spectra as a function of time.

In this paper, we predict the light curves and spectra of tidal disruption events as a function of time. Since the early work on tidal disruption (e.g., Rees 1988), it has been well-appreciated that the bulk of the emission occurs in the UV and soft X-rays, with a possible extension to harder X-rays.¹ Taking into account only this emission, optical wavelengths are not the most promising for detecting tidal flares, because the blackbody temperature of the inner accretion disk is $\sim 3 \times 10^5 \text{ K}$. We show, however, that there are two additional sources of optical emission that likely dominate the optical flux in many, though not all, cases: (1) emission produced by a super-Eddington outflow at early times and (2) emission produced by the irradiation and photoionization of unbound stellar debris (see also the earlier work of Bogdanović et al. 2004). In the latter case, much of the optical emission is in the form of very broad emission lines, while in the former it is primarily continuum (although some lines may also be present). Throughout this paper, we typically discuss these two sources of emission separately, largely because the physics of the photoionized stellar debris is more secure than that of the super-Eddington outflows.

The remainder of this paper is organized as follows. In §§2.1, 2.2 and 3, we describe our models for the polar super-Eddington outflow, accretion disk and the equatorial unbound material, respectively; then in §4 we calculate the luminosity and spectral signatures of tidal disruption events. We predict detection rates in §5, and summarize and discuss our results in §6. §§5.2 and 6 include a discussion of our models in the context of ROSAT and GALEX observations of tidal flare candidates.

2 THE INITIALLY BOUND MATERIAL

We consider a star approaching the BH on a parabolic orbit with pericenter distance $R_p \leq R_T$. Once the star reaches the vicinity of the tidal radius (R_T), the tidal gravity stretches it radially and compresses it vertically and azimuthally. The acceleration is $a \sim (GM_{\text{BH}}/R_p^2)(R_*/R_p)$ and acts for a dynamical time $t_p \sim (GM_{\text{BH}}/R_p^3)^{-1/2}$ near pericenter, resulting in velocity perturbations $\Delta v_p \sim at_p \sim v_*(R_T/R_p)^{3/2}$,

where R_* is the star's radius and v_* is the star's escape velocity. The change in velocity Δv_p is smaller than the star's orbital velocity at pericenter, $v_p \equiv (2GM_{\text{BH}}/R_p)^{1/2}$, by a factor of R_*/R_p .

Because Δv_p is at least as large as the sound speed inside the star, the stellar gas may shock vertically and azimuthally (e.g., Brassart & Luminet 2008; Guillochon et al. 2008). Once the shredded star passes through pericenter, the compression subsides and the star re-expands, cooling adiabatically; thermal pressure becomes negligible and the particles travel away from the BH ballistically. We assume that the particle trajectories become ballistic when the star passes through pericenter. At that time, the particles have perturbed azimuthal, vertical, and radial velocities $\sim \Delta v_p$.

The particles have a range in specific energy $\mathcal{E} \sim \pm 3(GM_{\text{BH}}/R_p)(R_*/R_p)$ (e.g., Lacy et al. 1982; Li et al. 2002), due to their relative locations in the BH's potential well and differences in their azimuthal speeds. Initially, approximately half of the stellar mass is bound and half is unbound (Lacy et al. 1982; Evans & Kochanek 1989). After a time

$$\begin{aligned} t_{\text{fallback}} &\sim \frac{2\pi}{6^{3/2}} \left(\frac{R_p}{R_*}\right)^{3/2} t_p \\ &\sim 20M_6^{5/2} R_{p,3R_S}^3 r_*^{-3/2} \text{ min}, \end{aligned} \quad (1)$$

the most bound material returns to pericenter. (Here we have defined $M_6 \equiv M_{\text{BH}}/10^6 M_\odot$, $R_{p,3R_S} \equiv R_p/3R_S$, and $r_* \equiv R_*/R_\odot$.) Less bound gas follows, at a rate

$$\dot{M}_{\text{fallback}} \approx \frac{1}{3} \frac{M_*}{t_{\text{fallback}}} \left(\frac{t}{t_{\text{fallback}}}\right)^{-5/3} \quad (2)$$

(Rees 1988; Phinney 1989). There will be some deviations from this canonical $t^{-5/3}$ scaling at early times, depending on the precise structure of the star (Lodato et al. 2009; Ramirez-Ruiz & Rosswog 2009), but we use equation (2) for simplicity. As matter returns to pericenter, it shocks on itself, converting most of its bulk orbital energy to thermal energy (see Kochanek 1994). The viscous time is typically shorter than the fallback time, so at least some of the matter begins to accrete.

For $M_{\text{BH}} \lesssim \text{few} \times 10^7 M_\odot$, the mass fallback rate predicted by equations (1) & (2) can be much greater than the Eddington rate \dot{M}_{Edd} for a period of weeks to years; here $\dot{M}_{\text{Edd}} \equiv 10L_{\text{Edd}}/c^2$, L_{Edd} is the Eddington luminosity, and 0.1 is the assumed efficiency of converting accretion power to luminosity. The fallback rate only falls below the Eddington rate at a time

$$t_{\text{Edd}} \sim 0.1 M_6^{2/5} R_{p,3R_S}^{6/5} m_*^{3/5} r_*^{-3/5} \text{ yr}, \quad (3)$$

where $m_* \equiv M_*/M_\odot$. While the fallback rate is super-Eddington, the stellar gas returning to pericenter is so dense that it cannot radiate and cool. In particular, the time for photons to diffuse out of the gas is longer than both the inflow time in the disk and the dynamical time characteristic of an outflow. The gas is likely to form an advective accretion disk accompanied by powerful outflows (e.g., Ohsuga et al. 2005), although the relative importance of accretion and outflows in this phase is somewhat uncertain (see §6). Later, when $\dot{M}_{\text{fallback}} < \dot{M}_{\text{Edd}}$ ($t > t_{\text{Edd}}$), the outflows subside, and the accretion disk can radiatively cool and becomes thin.

In §2.1, we describe our model for the super-Eddington

¹ Such a hard X-ray component may be detectable with upcoming all-sky X-ray surveys like the proposed EXIST mission (Grindlay 2004). However, we choose not to include predictions for hard X-rays in our calculations: one could draw analogy to the hard X-ray power-law tail observed in AGN spectra, but since the origin of this feature is uncertain, it is difficult to make firm theoretical predictions for tidal disruption events.

outflows, and in §2.2, we describe our model for the accretion disk. We discuss uncertainties in these models in §6.

2.1 Super-Eddington Outflows

When the fallback rate to pericenter is super-Eddington, radiation produced by the shock and by viscous stresses in the rotating disk is trapped by electron scattering. By energy conservation, this material is initially all bound to the BH, but it is only weakly bound because the radiation cannot escape and because the material originated on highly eccentric orbits. Some fraction of the returning gas is thus likely unbound (see, e.g., the simulations of Ayal et al. 2000), with energy being conserved as other gas accretes inward (Blandford & Begelman 1999). If the outflow's covering fraction is high, most of the radiated power will be emitted from the outflow's photosphere, which can be far outside $\sim R_p$ (Loeb & Ulmer 1997). We now estimate the properties of this outflowing gas (see Rossi & Begelman 2009 for related estimates in the context of short-duration gamma-ray bursts).

In our simplified scenario, stellar debris falls back at close to the escape velocity and shocks at the launch radius $R_L \sim 2R_p$, converting bulk kinetic energy to radiation:

$$aT_L^4 \sim \frac{1}{2}\rho_{\text{fallback,L}}v_{\text{esc,L}}^2, \quad (4)$$

where T_L is the temperature at R_L , $\rho_{\text{fallback,L}} \sim \dot{M}_{\text{fallback}}/(4\pi R_L^2 v_{\text{esc,L}})$ is the density of gas at R_L , and $v_{\text{esc,L}} \equiv (2GM_{\text{BH}}/R_L)^{1/2}$. Outflowing gas is launched from R_L at a rate

$$\dot{M}_{\text{out}} \equiv f_{\text{out}}\dot{M}_{\text{fallback}} \quad (5)$$

and with terminal velocity

$$v_{\text{wind}} \equiv f_v v_{\text{esc}}(R_L). \quad (6)$$

We approximate the outflow's geometry as spherical, with a density profile

$$\rho(r) \sim \frac{\dot{M}_{\text{out}}}{4\pi r^2 v_{\text{wind}}} \quad (7)$$

inside the outflow where $r \lesssim R_{\text{edge}} \equiv v_{\text{wind}}t$; the density falls quickly to zero at $\sim R_{\text{edge}}$. We define the trapping radius R_{trap} via $R_{\text{trap}}\rho(R_{\text{trap}})\kappa_s \sim c/v_{\text{wind}}$ (where κ_s is the opacity due to electron scattering): inside R_{trap} , the gas is too optically thick for photons to escape and so the outflowing gas expands adiabatically. Because the outflow remains supported by radiation pressure, $T \propto \rho^{1/3}$. The photosphere of the outflow R_{ph} is where $R_{\text{ph}}\rho(R_{\text{ph}})\kappa_s \sim 1$. Because v_{wind} is likely not much smaller than c , $R_{\text{trap}} \sim R_{\text{ph}}$; we thus neglect any deviations from adiabaticity between R_{trap} and R_{ph} .

At the earliest times for small M_{BH} and R_p , the fallback rate can be so large and the density so high that the edge of the outflow limits the location of the photosphere to be just inside R_{edge} . In that case, the density of the photosphere is still given by $\rho(R_{\text{ph}}) \sim (\kappa_s R_{\text{edge}})^{-1}$; lacking a detailed model, we assume that the photospheric gas near the edge is on the same adiabat as the rest of the gas, so that

$$T_{\text{ph}} \sim T_L \left[\frac{\rho(R_{\text{ph}})}{\rho_{\text{fallback,L}}} \right]^{1/3} \quad (8)$$

$$\sim 3 \times 10^4 f_v^{-1/3} M_6^{1/36} R_{p,3R_S}^{-1/8} m_\star^{-1/12} r_\star^{1/12} \left(\frac{t}{\text{day}} \right)^{-7/36} \text{ K}.$$

Note that the photospheric temperature during the edge-dominated phase is essentially independent of all parameters of the disruption (e.g., M_{BH} , R_p , etc.), and is only a weak function of time. The total luminosity during this phase grows as $L \propto t^{11/9}$ while the luminosity on the Rayleigh-Jeans tail increases even more rapidly, $\nu L_\nu \propto t^{65/36}$. After a time

$$t_{\text{edge}} \sim 1 f_{\text{out}}^{3/8} f_v^{-3/4} M_6^{5/8} R_{p,3R_S}^{9/8} m_\star^{3/8} r_\star^{-3/8} \text{ day}, \quad (9)$$

the density falls sufficiently that the photosphere lies well inside R_{edge} ; the photosphere's radius is then

$$R_{\text{ph}} \sim 4 f_{\text{out}} f_v^{-1} \left(\frac{\dot{M}_{\text{fallback}}}{\dot{M}_{\text{Edd}}} \right) R_{p,3R_S}^{1/2} R_S \quad (10)$$

and its temperature is

$$T_{\text{ph}} \sim 2 \times 10^5 f_{\text{out}}^{-1/3} f_v^{1/3} \left(\frac{\dot{M}_{\text{fallback}}}{\dot{M}_{\text{Edd}}} \right)^{-5/12} M_6^{-1/4} R_{p,3R_S}^{-7/24} \text{ K}. \quad (11)$$

The adiabatically expanding outflow preserves the photon distribution function generated in the shock and accretion disk close to the BH. Estimates indicate that this gas is likely to be close to thermal equilibrium and thus we assume that the escaping photons have a blackbody spectrum

$$\nu L_\nu \sim 4\pi^2 R_{\text{ph}}^2 \nu B_\nu(T_{\text{ph}}). \quad (12)$$

When the photosphere lies inside the edge of the outflow (i.e., $t > t_{\text{edge}}$ so $R_{\text{ph}} < v_{\text{wind}}t$), equations (10) and (11) imply that the total luminosity of the outflow is

$$L \sim 10^{44} f_{\text{out}}^{2/3} f_v^{-2/3} M_6^{11/9} R_{p,3R_S}^{1/2} m_\star^{1/3} r_\star^{-1/3} \left(\frac{t}{\text{day}} \right)^{-5/9} \text{ erg s}^{-1}. \quad (13)$$

The total luminosity of the outflow is thus of order the Eddington luminosity: see Figure 4, discussed in §4.1. Note that the total luminosity decreases for lower outflow rates, $L \propto f_{\text{out}}^{2/3}$, because the photosphere's surface area is smaller. The luminosity on the Rayleigh-Jeans tail (generally appropriate for optical and near-infrared wavelengths) declines even faster for lower \dot{M}_{out} , scaling as

$$\nu L_\nu \propto f_{\text{out}}^{5/3} f_v^{-5/3}. \quad (14)$$

These relations only apply if $R_{\text{ph}} \gtrsim R_L$ because otherwise the outflow is optically thin; we impose this lower limit to R_{ph} in our numerical solutions described later.

2.2 The Accretion Disk

We now consider the bound stellar debris that accretes onto the BH. After shocking at pericenter, this gas circularizes and viscously drifts inward, forming an accretion disk. The disk extends from $\sim 2R_p$ down to the last stable orbit, R_{LSO} . We expect the viscous time in the disk to be substantially shorter than the fallback time for at least a few years (see Ulmer 1999 for the case of $R_p = R_T$, assuming a thick disk), and check this expectation at the end of §2.2; we thus assume that accretion during this period proceeds at $\dot{M} \simeq (1 - f_{\text{out}})\dot{M}_{\text{fallback}}$. During the super-Eddington phase, the time for photons to diffuse out of the disk is longer than the viscous time, and so the disk is thick and advective. In

contrast, at later times when $\dot{M}_{\text{fallback}} \lesssim \dot{M}_{\text{Edd}}$, the disk is thin and can cool by radiative diffusion. We derive an analytic “slim disk” model (similar to the numerical work of Abramowicz et al. 1988) to describe the structure of the disk in both regimes.

To calculate the disk’s properties, we solve the equations of conservation of mass, momentum, and energy:

$$\dot{M} = -4\pi R H \rho v_r, \quad (15)$$

$$v_r = -\frac{3}{2} \frac{\nu}{R} \frac{1}{f}, \quad (16)$$

$$q^+ = q^- - \rho T v_r \frac{s}{R}, \quad (17)$$

where we have approximated the radial entropy gradient as $\partial s / \partial R \sim -s / R$. Here \dot{M} is the accretion rate, R is the cylindrical distance from the BH, H is the disk scale height, ρ is the density, v_r is the radial velocity, and T is the mid-plane temperature. The no-torque boundary condition at the inner edge of the disk implies $f \equiv 1 - (R_{\text{LSO}}/R)^{1/2}$. We neglect gas pressure, since radiation pressure is dominant throughout the disk for at least a few years; we further assume that the viscous stress is proportional to the radiation pressure, so that (Shakura & Sunyaev 1973) $\nu = \alpha c_s H$ with sound speed $c_s = (aT^4/3\rho)^{1/2}$ and $H = c_s/\Omega_K$, where $\Omega_K \equiv (GM_{\text{BH}}/R^3)^{1/2}$. Simulations indicate that this assumption is reasonable and that such disks are thermally stable (Hirose et al. 2009). The vertically integrated heating and cooling rates are given by $2Hq^+ = 3GM_{\text{BH}}\dot{M}f/4\pi R^3$ and $2Hq^- = 8\sigma T^4/3\tau$, where the half-height optical depth is $\tau = H\rho\kappa_s$ and κ_s is the electron scattering opacity. These relations form a quadratic equation for the dimensionless quantity $\kappa_s a T^4 / c \Omega_K = 3\tau(c_s/c)$,

$$0 = \left(\frac{\kappa_s a T^4}{c \Omega_K} \right)^2 - \frac{4}{3\alpha} \left(\frac{\kappa_s a T^4}{c \Omega_K} \right) - \frac{8f}{3\alpha^2} \left(\frac{10\dot{M}}{\dot{M}_{\text{Edd}}} \right)^2 \left(\frac{R}{R_S} \right)^{-2}. \quad (18)$$

Solving equation (18) yields the effective temperature of the disk,

$$\sigma T_{\text{eff}}^4 = \frac{4\sigma T^4}{3\tau} = \frac{3GM_{\text{BH}}\dot{M}f}{8\pi R^3} \times \left[\frac{1}{2} + \left\{ \frac{1}{4} + \frac{3}{2}f \left(\frac{10\dot{M}}{\dot{M}_{\text{Edd}}} \right)^2 \left(\frac{R}{R_S} \right)^{-2} \right\}^{1/2} \right]^{-1}. \quad (19)$$

Combining this relation with equation (2), we calculate the luminosity and spectrum of the disk as a function of time, modeling it as a multicolor blackbody.

The solution to (18) also yields the disk scale height ratio,

$$\frac{H}{R} = \frac{3}{4}f \left(\frac{10\dot{M}}{\dot{M}_{\text{Edd}}} \right) \left(\frac{R}{R_S} \right)^{-1} \times \left[\frac{1}{2} + \left\{ \frac{1}{4} + \frac{3}{2}f \left(\frac{10\dot{M}}{\dot{M}_{\text{Edd}}} \right)^2 \left(\frac{R}{R_S} \right)^{-2} \right\}^{1/2} \right]^{-1}. \quad (20)$$

The scale height $H \sim R$ while $\dot{M}_{\text{fallback}} \gtrsim \dot{M}_{\text{Edd}}$, and decreases as $t^{-5/3}$ at fixed R at later times. The viscous time at a radius R in the disk is

$$t_{\text{visc}} \sim \alpha^{-1} \left(\frac{GM_{\text{BH}}}{R^3} \right)^{-1/2} \left(\frac{H}{R} \right)^{-2}, \quad (21)$$

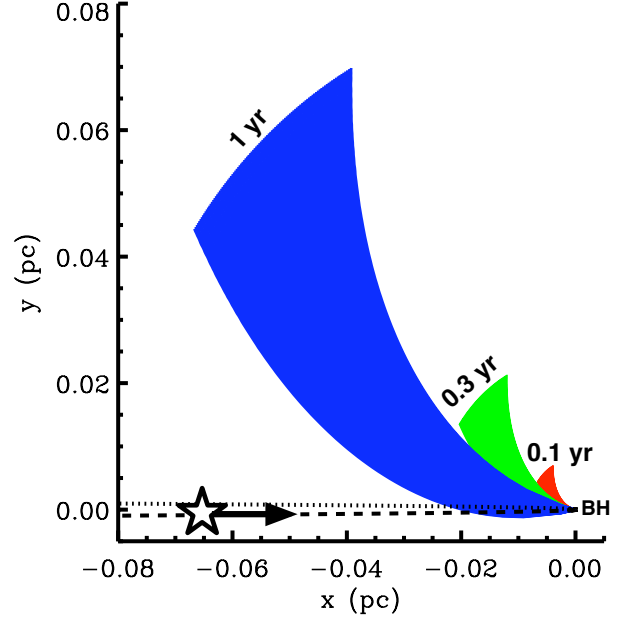


Figure 1. Spatial diagram of the equatorial stellar debris in the plane defined by the original orbit of the star. The unbound material is shown 0.1 yr, 0.3 yr, and 1 yr after the tidal disruption of a solar-type star by a $10^6 M_{\odot}$ BH at $R_p = 3R_S$. The dashed and dotted curves indicate the incoming parabolic trajectory of the star and its continuation if the star were not disrupted. The debris also has an inclination dispersion perpendicular to this plane of $\Delta i \sim 2R_{\star}/R_p$.

which is $\sim \alpha^{-1}$ times the local dynamical time during the super-Eddington phase, and later increases as $t^{10/3}$ at fixed R . For $\alpha \sim 0.1$, the viscous timescale evaluated at the disk’s outer edge is shorter than the time t since disruption for $\sim 1 - 3$ yr; our assumption of steady-state accretion during this period is thus consistent.

3 THE EQUATORIAL UNBOUND MATERIAL

While half of the initial star becomes bound to the BH during the disruption, the other half gains energy and escapes from the BH on hyperbolic trajectories. From the viewpoint of the BH, this unbound material subtends a solid angle $\Delta\Omega$, with a dispersion $\Delta\phi$ in azimuth and a dispersion Δi in orbital inclination. This material absorbs and re-radiates a fraction of the luminosity from the accretion disk.² We now estimate the dimensions of the unbound wedge.

In the orbital plane at a fixed time $t \gtrsim t_{\text{fallback}}$, the unbound stellar debris lies along an arc, as the spread in specific energy produces a spread in radius and azimuthal angle (see Fig. 1). The most energetic particles escape on a hyperbolic orbit with eccentricity $e_{\text{max}} \sim 1 + 6R_{\star}/R_p$. These particles race away from the BH at a substantial fraction of the speed of light,

² The polar outflow could also irradiate the unbound material, but it will have less of an effect because its spectrum is softer and its luminosity declines more rapidly.

$$\frac{v_{\max}}{c} \sim \left(\frac{3R_{\star}}{R_p}\right)^{1/2} \frac{v_p}{c} \sim 0.3M_6^{-1/2} R_{p,3R_S}^{-1} \quad (22)$$

(ignoring relativistic effects) and lie furthest from the BH at a distance

$$R_{\max} \sim 0.01M_6^{-1/2} R_{p,3R_S}^{-1} r_{\star}^{1/2} \left(\frac{t}{0.1 \text{ yr}}\right) \text{ pc}. \quad (23)$$

They also have the smallest angle away from stellar pericenter, $\phi_{\min} \sim f_{\infty}$, where f_{∞} obeys $\cos f_{\infty} = -1/\epsilon_{\max}$ so that $\phi_{\min} \sim \pi - (12R_{\star}/R_p)^{1/2}$ (see also Khokhlov & Melia 1996). Particles with lower energies and thus smaller eccentricities are closer to the BH and make a larger angle relative to pericenter, up to $\phi \sim \pi$. This produces an azimuthal dispersion $\Delta\phi \sim (12R_{\star}/R_p)^{1/2}$.

Particles having the maximum vertical velocity Δv_p have vertical specific angular momentum $j_z = R_p v_p$, and total specific angular momentum

$$j \sim R_p v_p \left[1 + \frac{1}{2} \left(\frac{\Delta v_p}{v_p}\right)^2\right] \sim R_p v_p \left[1 + \frac{1}{2} \left(\frac{R_{\star}}{R_p}\right)^2\right] \quad (24)$$

to lowest order in $\Delta v_p/v_p$. The orbital inclination i is given by $\cos i = j_z/j \sim 1 - (1/2)(R_{\star}/R_p)^2$, so $i \sim \pm R_{\star}/R_p$. The resulting inclination dispersion is $\Delta i \sim 2R_{\star}/R_p$ (our result is consistent with Evans & Kochanek 1989 but we disagree with Khokhlov & Melia 1996).

The finite inclination dispersion produces a vertical wall of debris whose inside face scatters, absorbs, and re-radiates a fraction of the disk's emission. This face subtends a solid angle

$$\begin{aligned} \Delta\Omega = \Delta i \Delta\phi &\sim 48^{1/2} \left(\frac{R_{\star}}{R_p}\right)^{3/2} \\ &\sim 0.2M_6^{-3/2} R_{p,3R_S}^{-3/2} r_{\star}^{3/2} \text{ sr}. \end{aligned} \quad (25)$$

The number density of particles in the unbound wedge is $n \sim (M_{\star}/2m_p)/(R^2\Delta R\Delta\Omega/3)$, where ΔR is the radial dispersion of the material at fixed ϕ . This dispersion is due to differences in the particles' radial velocities and azimuthal positions when the star passes through pericenter. Particles at $\sim R_{\max}$ travel on orbits whose pericenter is shifted from the star's pericenter by an angle $\sim \pm 3(R_{\star}/R_p)$, which produces a spread in radial position $(\Delta R/R)_{\max} \sim (3R_{\star}/R_p)^{1/2}$. The number density is then

$$n \sim 10^9 M_6^{7/2} R_{p,3R_S}^5 m_{\star} r_{\star}^{-7/2} \left(\frac{t}{0.1 \text{ yr}}\right)^{-3} \text{ cm}^{-3} \quad (26)$$

and the radial column density seen by the black hole is

$$N \sim 10^{25} M_6^{5/2} R_{p,3R_S}^{7/2} m_{\star} r_{\star}^{-5/2} \left(\frac{t}{0.1 \text{ yr}}\right)^{-2} \text{ cm}^{-2}. \quad (27)$$

As the unbound material expands, it cools very quickly; after at most a few weeks, the gas would all be neutral if not for the disk's ionizing radiation. This radiation ionizes the surface layer of the unbound material. The ionized gas in turn emits via bremsstrahlung, radiative recombination, and lines. The physical conditions and processes here are similar to those in the broad line region of an active galactic nucleus (AGN).

The ionized gas can reach photoionization equilibrium provided conditions change more slowly than the hydrogen

recombination rate $t_{\text{rec}}^{-1} \sim n_e \alpha_{\text{rec}}$. The recombination coefficient for hydrogen is $\alpha_{\text{rec}} \approx 4 \times 10^{-13} \text{ cm}^3 \text{ s}^{-1}$, and n_e is the electron number density. In the ionized region, $n_e/n \approx 1$, as we show below. The material can remain in equilibrium for at least a few years, until $t_{\text{rec}}/t \gtrsim 1$:

$$\frac{t_{\text{rec}}}{t} \sim (n\alpha_{\text{rec}}t)^{-1} \sim 10^{-3} M_6^{-7/2} R_{p,3R_S}^{-5} m_{\star}^{-1} r_{\star}^{7/2} \left(\frac{t}{0.1 \text{ yr}}\right)^2. \quad (28)$$

The column depth of the ionization front is $N_{\text{ion}} \sim 10^{23} U \text{ cm}^{-2}$, where $U \equiv L_{\text{disk}}/4\pi R_{\text{max}}^2 c \langle h\nu \rangle n$ is the ionization parameter,

$$U \sim \quad (29)$$

$$0.3 \left(\frac{L_{\text{disk}}}{L_{\text{Edd}}}\right) \left(\frac{\langle h\nu \rangle}{0.1 \text{ keV}}\right)^{-1} M_6^{-3/2} R_{p,3R_S}^{-3} m_{\star}^{-1} r_{\star}^{5/2} \left(\frac{t}{0.1 \text{ yr}}\right).$$

The electron density in the ionized layer is $n_e \approx n(1 - 10^{-6}U^{-1}) \approx n$ and the fractional depth of the ionization front is

$$\frac{\Delta R_{\text{ion}}}{\Delta R} = \frac{N_{\text{ion}}}{N} \sim$$

$$3 \times 10^{-3} \left(\frac{L_{\text{disk}}}{L_{\text{Edd}}}\right) \left(\frac{\langle h\nu \rangle}{0.1 \text{ keV}}\right)^{-1} M_6^{-4} R_{p,3R_S}^{-13/2} m_{\star}^{-2} r_{\star}^5 \left(\frac{t}{0.1 \text{ yr}}\right)^3, \quad (30)$$

so the ionized layer is typically thin and highly ionized.

4 PREDICTED EMISSION

We use the results of §§2 and 3 to calculate the emission due to the tidal disruption of a solar-type star as a function of time and wavelength. We consider a solar-type star because the stellar mass-radius relation and typical stellar mass functions imply that these stars should dominate the event rate. The two key parameters we vary are the star's pericenter distance R_p and the BH mass M_{BH} . We consider the mass range $M_{\text{BH}} \sim 10^5 - 10^8 M_{\odot}$.

4.1 Super-Eddington Outflows

Early on, when $\dot{M}_{\text{fallback}} \gtrsim \dot{M}_{\text{Edd}}$ ($t < t_{\text{Edd}}$), outflowing gas likely dominates the emission. We calculate its properties using results from §2.1.

In Figure 2 we plot the spectral energy distribution at various times during the outflow phase, for three fiducial models: $M_{\text{BH}} = 10^6 M_{\odot}$ and $R_p = 3R_S$; $M_{\text{BH}} = 10^6 M_{\odot}$ and $R_p = R_T$; and $M_{\text{BH}} = 10^7 M_{\odot}$ and $R_p = R_T$. We take nominal values of $f_v = 1$ and $f_{\text{out}} = 0.1$; we discuss the uncertainties in these parameters in §§5.3 and 6. The photosphere lies well inside the edge of the outflow at all times shown in Figure 2. The emission from the outflow has a blackbody spectrum, initially peaking at optical/UV wavelengths. As time passes and the density of the outflow subsides, the photosphere recedes and the emission becomes hotter but less luminous.

In Figure 3, we plot g - (4770Å) and i - (7625Å) band light curves for the three fiducial models. In the leftmost panel at $t \lesssim 1$ day, the edge of the outflow limits the size of the photosphere, so the photosphere initially expands, following the edge of the outflow. After a time t_{edge} (eq. [9]), however, the photosphere begins to recede inside the edge

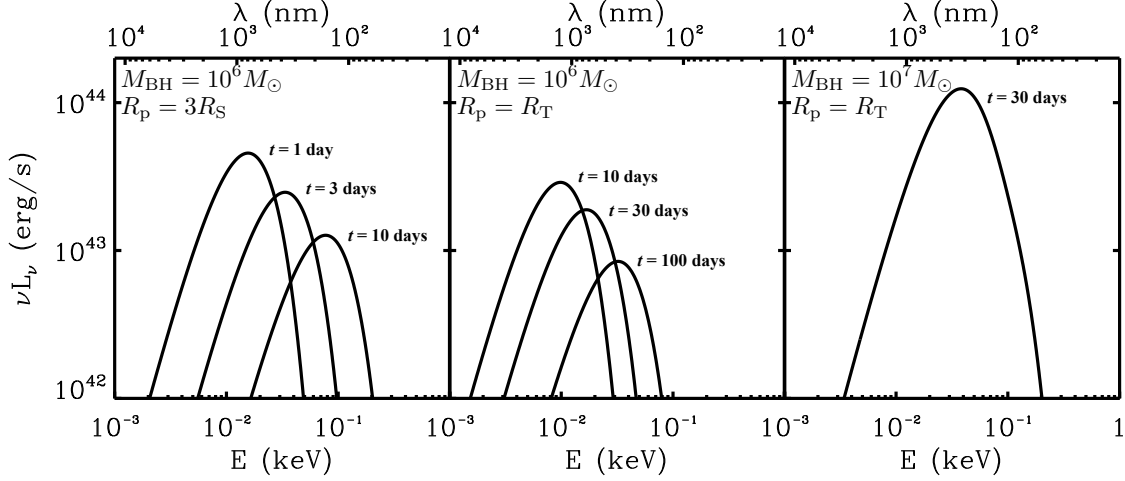


Figure 2. Spectral energy distributions for our three fiducial tidal disruption flares at several different times after disruption. These spectra include only the emission from the super-Eddington outflows (for $f_{\text{out}} = 0.1$ and $f_v = 1$; see eqns [5] & [6]), which dominate the emission at early times (see Fig. 3). For $M_{\text{BH}} = 10^7 M_{\odot}$ and $R_p = R_T$ (right panel), the disk dominates the emission for $t \gtrsim 50$ days (Fig. 3); this is why we do not plot the outflow emission at later times.

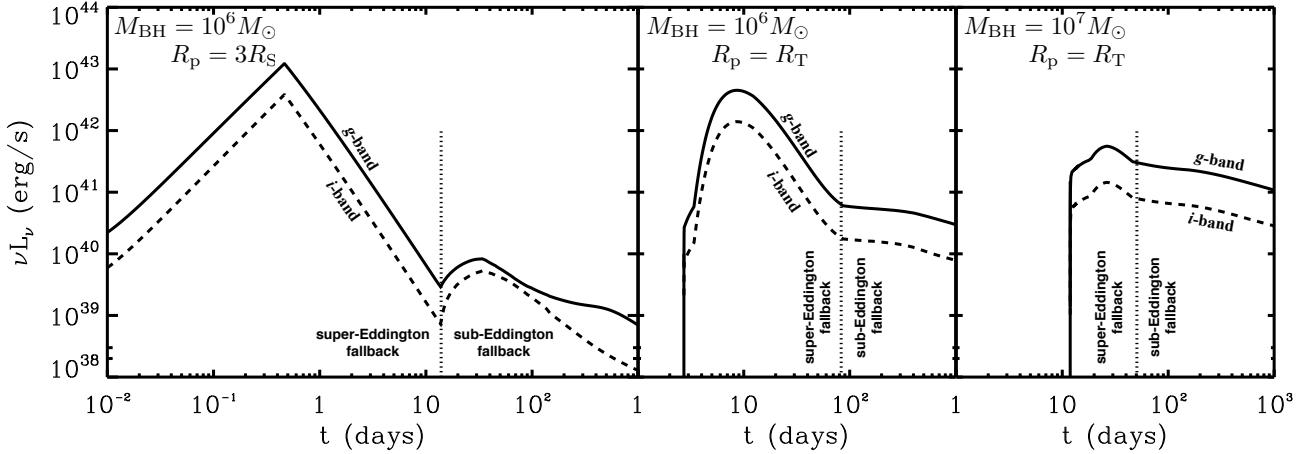


Figure 3. Light curves at g - (solid) and i -band (dashed) for our three fiducial models. In each panel, times to the left of the vertical dotted line ($\sim t_{\text{Edd}}$; eq. [3]) have super-Eddington fallback rates and an outflow dominates the optical emission; at later times, the fallback rate is sub-Eddington and the emission is produced by the accretion disk and the photoionized unbound material (see §4.2). In the leftmost panel, the emission rises at early times because the edge of the outflow limits the size of the photosphere. The optical emission then declines until the end of the outflow phase as the photosphere recedes and the photospheric temperature rises (Fig. 2).

of the outflow and the luminosity declines. In the middle and rightmost panels, the photosphere lies well inside R_{edge} for virtually the entire outflow phase. The optical emission decreases as the photosphere’s emitting area decreases and the temperature rises only slowly. As Figures 2 & 3 demonstrate, the peak optical luminosity of the outflow is substantial, $\sim 10^{43} \text{ erg s}^{-1} \sim 10^9 L_{\odot}$, comparable to the optical luminosity of a supernova. The color of the emission is quite blue ($g - r \approx -0.8$). To illustrate how the peak luminosity depends on the parameters of the disruption event, Figure 4 shows the peak bolometric and g -band luminosities of the outflow as a function of M_{BH} , for $R_p = 3R_S$ and $R_p = R_T$.

For sources at cosmological distances (which *are* detectable; §5), the negative k -correction associated with the Rayleigh-Jeans tail implies that the rest-frame g -band luminosity in Figure 4 underestimates the peak optical luminosity visible at Earth.

4.2 Disk and Photoionized Unbound Debris

When $\dot{M}_{\text{fallback}} \gtrsim \dot{M}_{\text{Edd}}$, a fraction of the falling-back gas is blown away while the remainder likely accretes via an advective disk (§2.2). As the fallback rate declines below Eddington, the photons are able to diffuse out of the region close

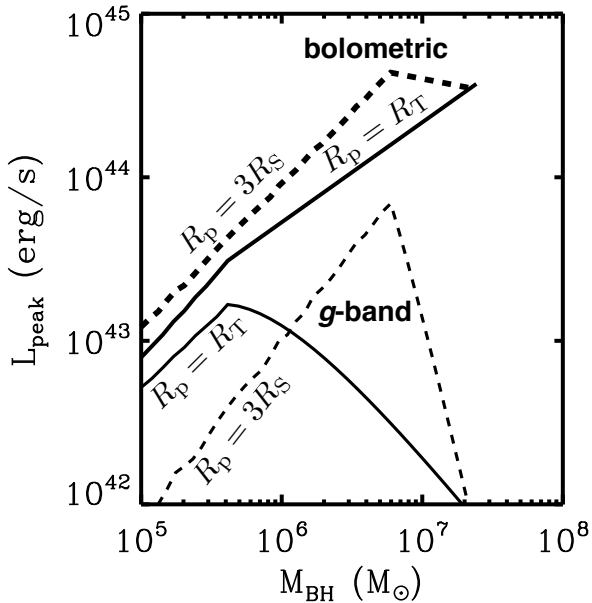


Figure 4. Peak bolometric (heavy lines) and g -band (light lines) luminosities of the early-time super-Eddington outflows as functions of M_{BH} , for $R_{\text{p}} = 3R_{\text{S}}$ (dashed) and $R_{\text{p}} = R_{\text{T}}$ (solid), assuming that $f_{\text{out}} = 0.1$ and $f_{\text{v}} = 1$. Figure 11 shows the duration of this phase.

to the BH and the disk cools efficiently, but also becomes less luminous. The vertical dotted line in Figure 3 delineates the super-Eddington fallback (and outflow) phase from the sub-Eddington fallback phase.

The accretion disk irradiates the surface of the equatorial unbound stellar material (§3). In this section we calculate the combined emission produced by the accretion disk and the irradiated stellar debris. In order to isolate the more theoretically secure emission by the disk and photoionized material, we do *not* consider the emission from super-Eddington outflows in this section. We show results for the disk and photoionized material at both $t < t_{\text{Edd}}$ and $t > t_{\text{Edd}}$; depending on the geometry of the outflow, and the viewing angle of the observer to the source, it is possible that all three emission components could be visible at early times. Because the mass driven away by outflows during the super-Eddington phase can also be photoionized by the central source at times $t > t_{\text{Edd}}$, our emission line predictions are likely a lower limit to the total emission line fluxes (§6).

We calculate the photoionization properties of the unbound material using version 07.02.02 of the publicly available code Cloudy, last described by Ferland et al. (1998). We simplify the geometry: the unbound spray traces out a widening spiral shape with most of the area coming from close to $\sim R_{\text{max}}$, so we approximate it as a cloud of area $R_{\text{max}}^2 \Delta\Omega$ located a distance R_{max} from the ionizing source. Our model cloud has constant density n (eq. [26]), column depth N (eq. [27]), and is irradiated by the accretion disk having the luminosity and spectrum described in §2.2. The total emission calculated here is the sum of the emission from this photoionized layer and the emission from the central accretion disk. We focus on non-rotating BHs

($R_{\text{LSO}} = 3R_{\text{S}}$), although we quote results for rapidly rotating holes ($R_{\text{LSO}} = R_{\text{S}}$) as well.

In Figure 5 we plot the spectral energy distribution 30 days, 100 days, 300 days, and 1000 days after disruption, for our three fiducial models: $M_{\text{BH}} = 10^6 M_{\odot}$ and $R_{\text{p}} = 3R_{\text{S}}$; $M_{\text{BH}} = 10^6 M_{\odot}$ and $R_{\text{p}} = R_{\text{T}}$; and $M_{\text{BH}} = 10^7 M_{\odot}$ and $R_{\text{p}} = R_{\text{T}}$. The early-time short-wavelength peaks at ~ 0.1 keV with luminosity $\sim L_{\text{Edd}}$ are emission from the disk. After a time t_{Edd} , the mass fallback rate declines below the Eddington rate, and the disk begins to cool and fade. For $R_{\text{p}} \sim R_{\text{LSO}}$ and $M_{\text{BH}} \sim 10^5 - 10^6 M_{\odot}$, the optical light is dominated by lines and continuum from the photoionized material. For larger M_{BH} (and larger $R_{\text{p}}/R_{\text{S}}$), the equatorial debris subtends a smaller solid angle (see eq. [25]) and the disk’s luminosity is larger, so the disk dominates the optical emission.

Figure 6 zooms in on the UV/optical/near-infrared spectra for our three fiducial models. The emission lines characteristic of the broad line region of an AGN are typically the strongest lines here as well: e.g., Ly α , CIV 1548+1551, H β , and H α . In most cases, these lines are optically thick for more than a year. The lines are extremely broad, since the marginally bound gas has a speed close to zero while the most energetic gas leaves the BH at $v_{\text{max}} \sim 0.4c$, $0.09c$, and $0.2c$ for $M_{\text{BH}} = 10^6 M_{\odot}$, $R_{\text{p}} = 3R_{\text{S}}$; $M_{\text{BH}} = 10^6 M_{\odot}$, $R_{\text{p}} = R_{\text{T}}$; and $M_{\text{BH}} = 10^7 M_{\odot}$, $R_{\text{p}} = R_{\text{T}}$, respectively (see eq. [22]). In addition, the mean velocity along our line of sight will usually be substantial, so the lines should have a large redshift or blueshift on top of the galaxy’s redshift. For clarity, we plot the spectra with a mean redshift of zero.

Figure 7 focuses on the evolution of five strong lines, plotting the ratio $L_{\nu,\text{line}}/L_{\nu,\text{cont}}$ at line center for each.³ The quantity $L_{\nu,\text{line}}$ is the line intensity at line center accounting for the significant broadening. As the surface area of the equatorial wedge grows in time, line luminosities grow until $\dot{M}_{\text{fallback}} \lesssim \dot{M}_{\text{edd}}$ and irradiation by the disk subsides. The quantity $L_{\nu,\text{cont}}$ is the continuum intensity, which includes the contributions of both the disk (blackbody) and the photoionized unbound material (bremsstrahlung and radiative recombination)—again, the emission from the super-Eddington outflows is not included in $L_{\nu,\text{cont}}$. The lines remain prominent for a few years, and are strongest and broadest for small M_{BH} and small $R_{\text{p}}/R_{\text{S}}$. The UV lines are the strongest lines when the unbound material dominates the continuum (left panel), while the near-infrared lines are the strongest when the disk dominates the continuum (middle and right panels).

We next describe the broadband optical evolution of a tidal disruption event. Figure 3, also discussed in §4.1, plots the optical light curve for each fiducial model, showing the total emission at both g - and i -bands. For $t \lesssim t_{\text{Edd}}$ (left of the dotted lines), the emission is dominated by the super-Eddington outflows, while for $t \gtrsim t_{\text{Edd}}$ the emission is dominated by the accretion disk and photoionized equatorial debris. Once $t > t_{\text{Edd}}$, i.e., $\dot{M}_{\text{fallback}} \lesssim \dot{M}_{\text{edd}}$, the disk’s optical luminosity falls off gently, approximately as $t^{-5/12}$:

³ By comparing the results of different versions of Cloudy, we find that the results for line strengths can be uncertain by up to factor few.

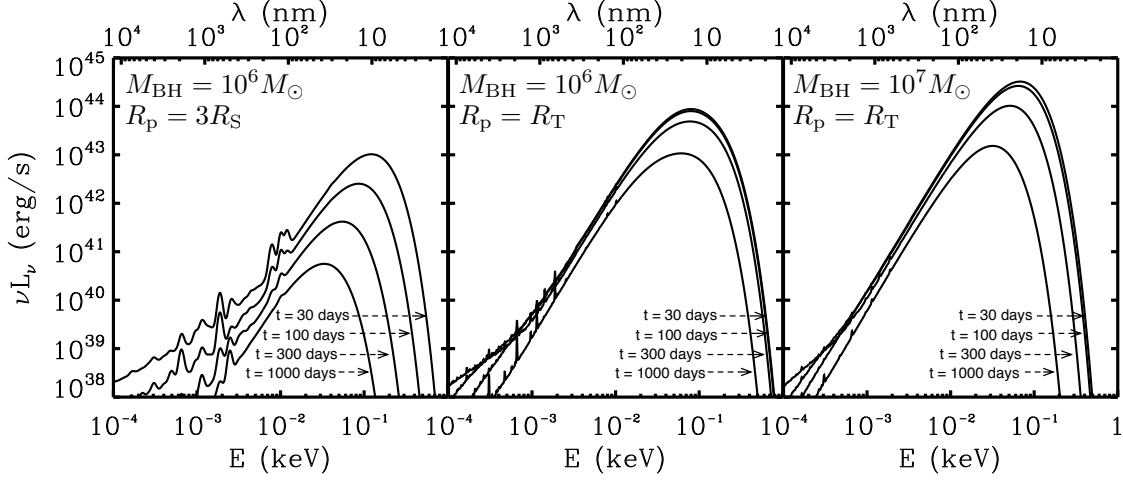


Figure 5. Spectral energy distributions for tidal flares around a non-rotating BH, 30, 100, 300, and 1000 days after disruption. Emission from the accretion disk dominates at short wavelengths. The photoionized unbound stellar debris absorbs and re-radiates some of the disk’s emission, producing optical-infrared emission. These spectra do not include the emission from super-Eddington outflows at early times; see Figs. 2 & 3 for this emission.

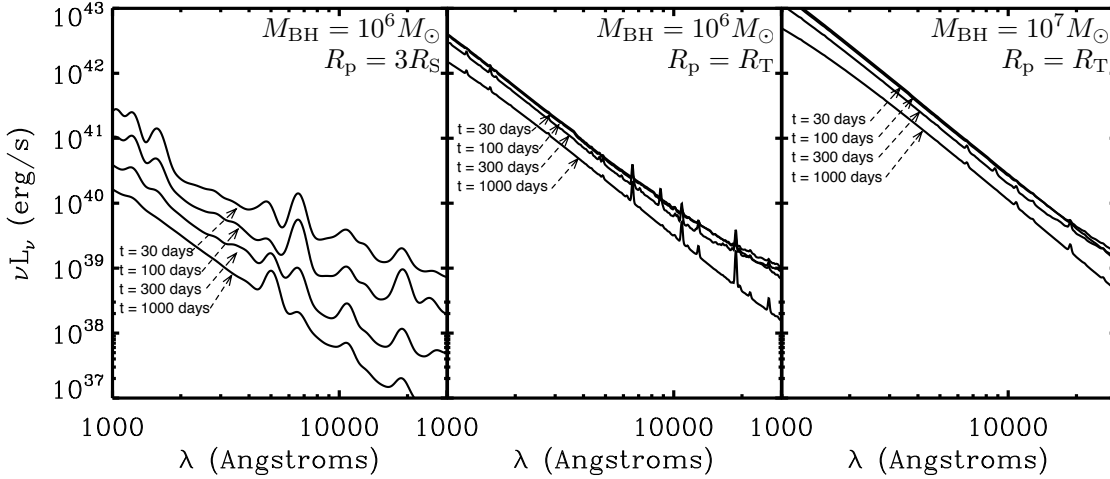


Figure 6. UV to near-infrared spectra for tidal flares around a non-rotating BH, 30, 100, 300, and 1000 days after disruption. The spectra are the sum of contributions from the accretion disk and the photoionized unbound material, but do not include the emission from super-Eddington outflows, which likely dominate at early times (Fig. 3). The linewidths and line strengths are both larger for smaller R_p/R_S and smaller M_{BH} (eq. [22]).

although the bolometric luminosity is declining as $t^{-5/3}$, the optical emission lies on the Rayleigh-Jeans tail. Increasing R_p/R_S and/or M_{BH} increases the disk’s luminosity by up to two orders of magnitude because of the disk’s larger emitting area and/or because L_{Edd} rises. At all times, the disk emission is quite blue ($g - r \approx -1$).

For large M_{BH} and/or large R_p/R_S (middle and right panels in Fig. 3), the disk outshines the photoionized material at optical wavelengths, and the light curves and color evolution are determined by the disk emission alone. By contrast, for $M_{BH} = 10^6 M_\odot$ and $R_p = 3R_S$ (left panel), the photoionized material’s optical line emission is initially an order of magnitude brighter than the disk. As the illumi-

nating power of the disk declines but the unbound debris becomes less dense, different lines wax and wane. The significant redshift or blueshift of the unbound material further complicates the photometry by altering which lines contribute in which wavebands (again, our figures assume a mean redshift of zero). These effects can produce a non-monotonic light curve and a complicated color evolution, depending on the exact redshift of the source and the velocity of the equatorial debris.

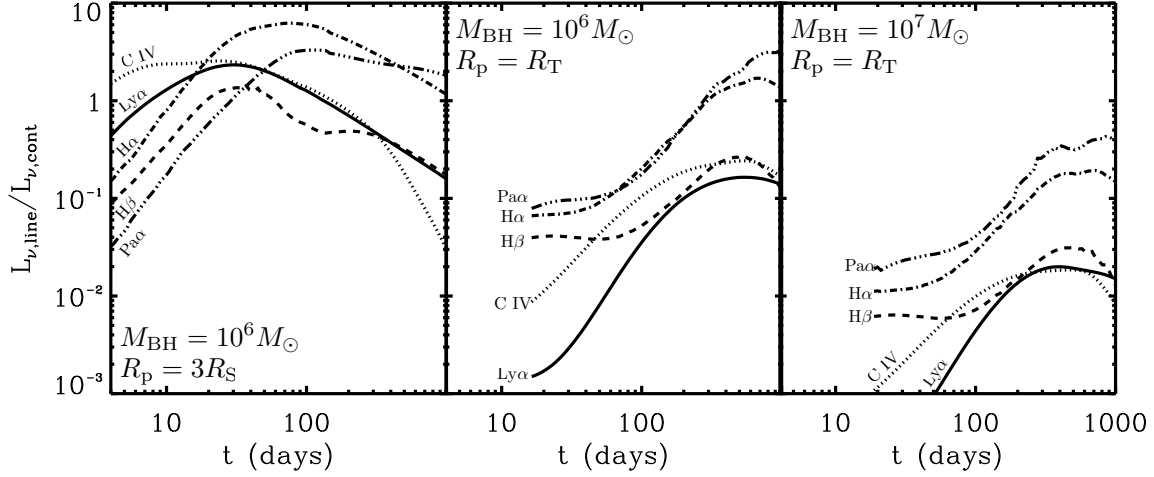


Figure 7. Line strength evolution for the three fiducial models. Results are shown for Ly α (solid), CIV 1548+1551 (dotted), H β (dashed), H α (dot-dashed), and Pa α (triple-dot-dashed). The quantity $L_{\nu, \text{line}}/L_{\nu, \text{cont}}$ is the ratio at line center of the line intensity to continuum intensity, taking into account emission from both the disk and the photoionized material, but not the early-time super-Eddington outflows.

Table 1. Assumed parameters for transient surveys⁴ and predicted rates. Our results can be scaled to other survey parameters and model assumptions using eq. (32).

Survey	f_{lim}	f_{sky}	Cadence	Rate: D+UB ^a (yr ⁻¹)	Rate: Outflows ^b (yr ⁻¹)
Pan-STARRS 3 π Survey	23 AB mag (g, i -band)	0.75	6 months	4 – 12	200
Pan-STARRS Medium Deep Survey (MDS)	25 AB mag (g -band)	2×10^{-3}	4 days	0.2 – 1	20
Palomar Transient Factory (PTF)	21 AB mag (g -band)	0.2	5 days	0.3 – 0.8	300
Large Synoptic Survey Telescope (LSST)	24.5 AB mag (g -band)	0.5	3 days	60 – 250	6000
Synoptic All-Sky Infrared Survey (SASIR) ^c	23.5 AB mag (Y -band)	0.03?	10 days?	0.1 – 0.5	100
ROSAT All-Sky Survey ^d	2×10^{-12} erg s ⁻¹ cm ⁻²	1	e	2 – 100	N/A ^f
GALEX Deep Imaging Survey	25 AB mag (2316 Å)	7×10^{-5}	e	0.05 – 0.2	N/A ^f

^a Rates for the emission from the disk and unbound equatorial debris; the range corresponds to $R_{\text{LSO}} = 3R_S$ (low), $R_{\text{LSO}} = 1R_S$ (high). This emission is relatively faint in the optical/infrared and may be difficult to detect relative to the host bulge (see §6).

^b Rates for the emission from super-Eddington outflows, restricted to $z < 1$, for $f_{\text{out}} = 0.1$ and $f_v = 1$ (see Fig. 13).

^c The survey strategy for SASIR has not yet been finalized.

^d These parameters are for comparison with the all-sky rate calculation by Donley et al. (2002).

^e ROSAT and GALEX do not have regular cadences.

^f ROSAT and GALEX have insufficient cadence and/or sky coverage to detect flares from super-Eddington outflows.

5 PREDICTED RATES

We use our calculated spectra and light curves to predict the number of tidal disruption events detectable by observational surveys. We focus on an (almost) all-sky optical survey like the Pan-STARRS PS1 3 π survey, but we also predict results for surveys with more rapid cadence (e.g., PTF and LSST) and discuss the results of our models compared to ROSAT and GALEX observations. Our assumed survey parameters are listed in Table 1, along with some of our results.⁴ Our results can readily be scaled to other surveys using equation (32) discussed below.

To predict rates, we use the redshift-dependent BH mass function given by Hopkins et al. (2007). At $z \sim 0$,

the BH density is $\simeq 10^{-2}$ Mpc⁻³ for $\sim 10^6 M_{\odot}$ and gently falling at higher masses; as z rises to 3, the BH number density falls by ~ 30 . We assume that the BH number density for $10^5 - 10^6 M_{\odot}$ is the same as for $\sim 10^6 M_{\odot}$, although it is poorly constrained observationally. We do not consider tidal disruption events beyond $z \sim 3$. (Our results can easily be scaled to other assumed BH mass densities; see eq. [32]).

The rate of tidal disruptions within a single galaxy is $\gamma(M_{\text{BH}})$. To predict detection rates, we assume that γ is independent of BH mass. We adopt $\gamma = 10^{-5}$ yr⁻¹ as found by Donley et al. (2002) using the ROSAT All-Sky Survey, which is also in line with conservative theoretical estimates. We further assume that this rate is distributed equally among logarithmic bins of stellar pericenter distance R_p , so that $d\gamma/d \ln R_p = \gamma / \ln(R_T/R_{p, \text{min}})$. In the limit of $z \ll 1$, the equation for the predicted rate is

⁴ These are intended to be illustrative, and may not correspond precisely to the true observational survey parameters, although we have attempted to be as accurate as possible.

$$\frac{d\Gamma}{d\ln M_{\text{BH}}} = \int_{R_{\text{p,min}}}^{R_{\text{T}}} \frac{4\pi}{3} d_{\text{max}}^3 f_{\text{sky}} \frac{dn}{d\ln M_{\text{BH}}} \frac{d\gamma}{d\ln R_{\text{p}}} d\ln R_{\text{p}} \quad (31)$$

where f_{sky} is the fraction of sky surveyed; when necessary we use the generalization of equation (31) that includes cosmological effects. When the duration of a flare t_{flare} is shorter than the cadence of the survey t_{cad} , we approximate the probability of detection as $t_{\text{flare}}/t_{\text{cad}}$.

We start by considering emission from only the accretion disk and photoionized equatorial debris. Then in §5.3, we include the emission from super-Eddington outflows, where the physics is somewhat less certain, but the observational prospects are particularly promising.

5.1 Disk and Photoionized Material

For all but the largest M_{BH} , the duration of peak optical emission for the accretion disk and photoionized material is $t_{\text{flare}} \sim t_{\text{Edd}}$ (eq. [3]). This timescale depends on the BH's mass and the star's pericenter distance, as shown in Figure 8. For $R_{\text{p}} \sim R_{\text{T}}$, the flare lasts for $t_{\text{Edd}} \sim 0.3 - 1$ yr and then decays only gently since the disk dominates the optical emission. However, for $M_{\text{BH}} \sim 10^5 - 10^6 M_{\odot}$ and $R_{\text{p}} \sim R_{\text{LSO}}$, the optical flare is shorter, $t_{\text{Edd}} \sim 0.03 - 0.1$ yr, and then the emission decays more quickly since irradiation of the unbound material—the dominant source of optical emission—subsides. For $M_{\text{BH}} \gtrsim 8 \times 10^7 M_{\odot}$, $t_{\text{flare}} \sim t_{\text{fallback}}$ (eq. [1]) because the fallback rate in these systems is never super-Eddington.

Figure 9 shows our calculated rates for optically-detected tidal flares (for a survey like the Pan-STARRS 3π survey), for both non-rotating and rapidly rotating BHs. For $M_{\text{BH}} \gtrsim 10^6 M_{\odot}$, the disk contributes most of the emitted power, so the rates increase with M_{BH} as $L_{\text{disk}} \sim L_{\text{Edd}}$ increases. The rates are dominated by $R_{\text{p}} \sim R_{\text{T}}$ and $M_{\text{BH}} \sim 2 \times 10^7 M_{\odot}$ (non-rotating BHs) and $M_{\text{BH}} \sim 10^8 M_{\odot}$ (rapidly rotating BHs). Since most of the flares that dominate the rates have relatively long durations (Fig. 8), imperfect survey cadence only modifies the detection rates by $\sim 50\%$. At $10^5 - 10^6 M_{\odot}$ and small R_{p} , the photoionized material re-emits a relatively large fraction of the disk's power in the optical and boosts the detection rates significantly.

Integrated over $M_{\text{BH}} = 10^6 - 10^8 M_{\odot}$, our estimated rates for the Pan-STARRS 3π survey, assuming non-rotating BHs, are 4 yr^{-1} and 2 yr^{-1} in g -band and i -band, respectively. The mass range $10^5 - 10^6 M_{\odot}$ contributes another 0.4 yr^{-1} (both g -band and i -band), assuming (probably optimistically) that $dn/d\ln M_{\text{BH}}$ and γ are the same at $10^5 M_{\odot}$ as at $10^6 M_{\odot}$. If the BH is rotating faster, $R_{\text{p}}/R_{\text{S}}$ can be smaller. This allows an accretion disk to form for even $M_{\text{BH}} \sim \text{few} \times 10^7 - 10^8 M_{\odot}$, widens the disk for all M_{BH} , and increases the solid angle of the unbound material. Indeed for $M_{\text{BH}} \sim 10^5 M_{\odot}$ and $R_{\text{p}} \sim R_{\text{S}}$, the unbound material covers a quarter of the sky! (At this point $R_{\text{S}} \sim R_{\odot}$ so our approximations begin to break down.) These effects raise the total predicted rates for rapidly rotating BHs to $\sim 12 \text{ yr}^{-1}$.

Figure 10 plots the detection rates as a function of $R_{\text{p}}/R_{\text{S}}$ for $M_{\text{BH}} = 10^5 M_{\odot}$, $10^6 M_{\odot}$, and $10^7 M_{\odot}$, for the disk alone (light lines) and for the disk plus photoionized material (heavy lines). The photoionized material enhances detection rates significantly for most $R_{\text{p}}/R_{\text{S}}$ at $10^5 M_{\odot}$ and $10^6 M_{\odot}$, but has little effect for $10^7 M_{\odot}$. The rates decrease

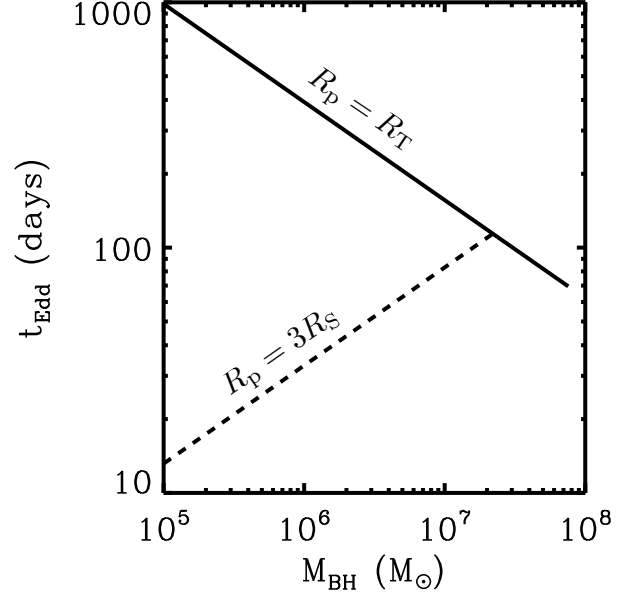


Figure 8. Duration of maximum luminosity during the late-time accretion disk phase, plotted as a function of M_{BH} for $R_{\text{p}} = 3R_{\text{S}}$ and $R_{\text{p}} = R_{\text{T}}$. Most flares last longer than \sim a month. The super-Eddington outflow at early times produces a shorter flare that should precede this emission (Figs. 3 & 11–13). (The fallback rates for $M_{\text{BH}} \gtrsim 8 \times 10^7 M_{\odot}$ are never super-Eddington, so the flare duration in these systems is $\sim t_{\text{fallback}}$.)

substantially for $R_{\text{p}}/R_{\text{S}} \rightarrow 1.5$ because then the outer radius of the disk $\simeq 2R_{\text{p}} = 3R_{\text{S}}$ is at the last stable orbit; our disk model assumes a no-torque boundary condition at R_{LSO} , implying that there is essentially no emission from the disk when $R_{\text{p}} \sim R_{\text{LSO}}$.

Although the rates quoted above and in Figures 9 and 10 are for a survey covering $3/4$ of the sky, assuming constant $\gamma(M_{\text{BH}})$ and constant BH mass density below $\simeq 10^6 M_{\odot}$, our predicted rates can be scaled to other assumed parameters:

$$\frac{d\Gamma}{d\ln M_{\text{BH}}} \propto f_{\text{lim}}^{-3/2} f_{\text{sky}} f_{\text{cad}} \frac{dn}{d\ln M_{\text{BH}}} \gamma(M_{\text{BH}}) \quad (32)$$

assuming that the sources are at $z \ll 1$, where $f_{\text{cad}} \equiv \min(t_{\text{flare}}/t_{\text{cad}}, 1)$.

The Pan-STARRS MDS, PTF, and LSST will have cadences of only a few days, giving them sensitivity to all events within their survey volumes. However, for detecting this relatively long-lived emission, the advantage of fast cadence is only minor; more significant is the spatial volume probed by the survey (see Table 1). The MDS will deeply ($m_{\text{AB}} \sim 25$) image a relatively small (84-deg^2) region, and so will detect $\sim 5 - 10\%$ as many events as the 3π Survey, $\sim 0.2 - 1$ per year. PTF will image a larger region (8000 deg^2) but less deeply ($m_{\text{AB}} \sim 21$), and so will have detection rates similar to the MDS. The emission from early-time super-Eddington outflows may significantly increase these rates, as we discuss in §5.3. In the next decade, LSST will image a large region ($20,000 \text{ deg}^2$) deeply ($m_{\text{AB}} \sim 24.5$), and so will discover hundreds of tidal flares. MDS and LSST will detect events at cosmological distances ($z_{\text{max}} \sim 0.3 - 0.6$), where the negative k-correction of the

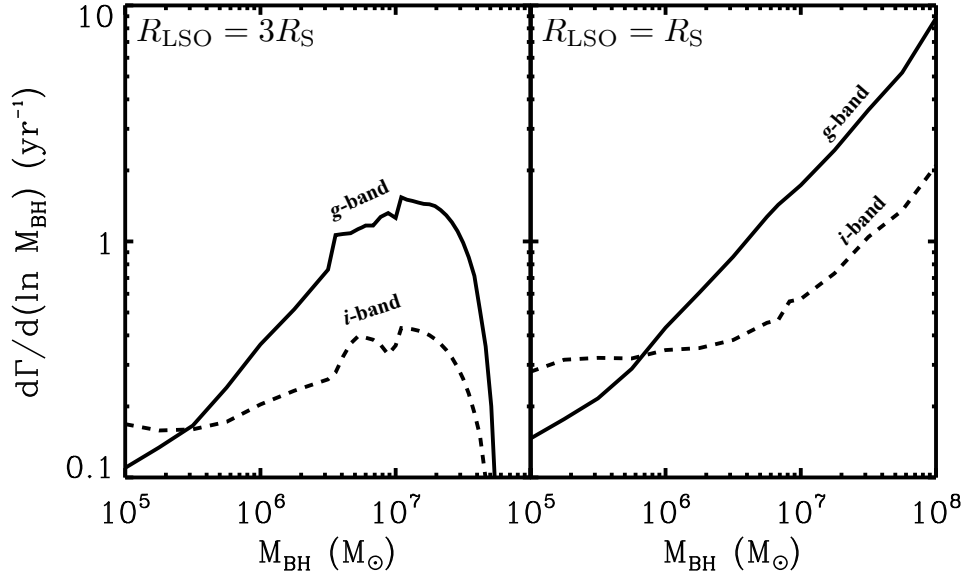


Figure 9. Predicted detection rates as a function of BH mass for the Pan-STARRS 3π survey (see Table 1). Results are shown for non-rotating BHs (left panel) and rapidly rotating BHs (right panel). The rates shown here can be scaled to other surveys and other model parameters using eq. (32). These rates do not include the emission from super-Eddington outflows at early times; see Figs. 12 & 13 for these results.

disk’s blackbody peak enhances rates by a factor of a few. By co-adding images up to ~ 1 month, these short-cadence surveys will also be able to raise their detection rates of events having $M_{\text{BH}} \sim 10^6 - 10^8 M_{\odot}$ by a factor of a few. Also in the next decade, SASIR plans to deeply image 140 deg^2 each night in the near infrared (to $m_{\text{AB}} \sim 23.5$ at Y-band; Bloom et al. 2009). Their observing strategy is not yet finalized; assuming a 10-day cadence covering 1400 deg^2 (a good strategy for detecting flares during the super-Eddington outflow phase; see §5.3), this survey should detect a flare every few years from the accretion disk plus photoionized debris.

5.2 Current Observational Constraints

As a check on our model, we have calculated rates for the ROSAT All-Sky Survey for comparison with Donley et al. (2002)’s result of 42 events per year over the whole sky for $f_{\text{lim}} = 2 \times 10^{-12} \text{ erg s}^{-1} \text{ cm}^{-2}$ ($0.2 - 2.4 \text{ keV}$).⁵ Considering blackbody emission alone, we predict 2 yr^{-1} ($R_{\text{in}} = 3R_{\text{S}}$) or 40 yr^{-1} ($R_{\text{in}} = R_{\text{S}}$). This strong sensitivity to R_{in} arises because the ROSAT band is on the Wien tail of the disk emission. If we assume that 10% of the emission is in an X-ray power-law tail with a photon index $\Gamma = 3$ (not unreasonable assumptions for X-ray emission from accreting BHs; e.g., Koratkar & Blaes 1999), our predicted rates are 10 yr^{-1} ($R_{\text{in}} = 3R_{\text{S}}$) and 100 yr^{-1} ($R_{\text{in}} = R_{\text{S}}$). Given the large uncertainties in the X-ray emission, our predictions are consistent with the observational results. We also compare with detection rates in the GALEX Deep Imaging Survey

(Gezari et al. 2008). They search an area of 2.882 square degrees, observed at FUV (1539 \AA) and NUV (2316 \AA) down to $f_{\text{lim}} \sim 25 \text{ AB}$ magnitudes. Gezari et al. detect 2 events⁶ in this region over 3 years. This is somewhat higher than our predicted rates in the NUV, 0.05 yr^{-1} if $R_{\text{in}} = 3R_{\text{S}}$ and 0.2 yr^{-1} if $R_{\text{in}} = R_{\text{S}}$ (assuming perfect cadence for simplicity), and may suggest that the disruption rate per galaxy γ is a factor of a few higher than we have assumed here.

As the above estimates demonstrate, consistency with GALEX and ROSAT constraints prefers a rate per galaxy of $\gamma \sim (1 - 3) \times 10^{-5} \text{ yr}^{-1}$. Significantly larger disruption rates, as some calculations predict (e.g., Merritt & Poon 2004), are inconsistent with current observational limits unless dust obscuration has significantly biased the ROSAT and GALEX results or the large disruption rates are confined to brief epochs in a galaxy’s life (e.g., a merger). Note also that this constraint only applies to massive BHs with $M_{\text{BH}} \sim 10^7 M_{\odot} - 10^8 M_{\odot}$, because UV and X-ray surveys select for these systems (§6).

5.3 Super-Eddington Outflows

We now calculate optical detection rates accounting for emission from the luminous but shorter-lived super-Eddington outflows. We begin by plotting the duration of peak emission for the outflow phase, $t_{\text{flare}} \sim t_{\text{outflow}}$, in Figure 11 as a function of M_{BH} for $R_{\text{p}} = 3R_{\text{S}}$ and $R_{\text{p}} = R_{\text{T}}$. For $R_{\text{p}} = 3R_{\text{S}}$ and $M_{\text{BH}} \lesssim 6 \times 10^6 M_{\odot}$, the duration of the outflow is set by the time at which the photosphere recedes inside the edge of the outflow ($t_{\text{outflow}} \sim t_{\text{edge}}$; eq. [9]) while for larger M_{BH} , the duration is set by the timescale for the most

⁵ The cadence is ~ 1 year but irregular; we assume it is perfect for simplicity. The rates we predict thus may be slightly high.

⁶ The candidate of Gezari et al. (2009) is in a different field.

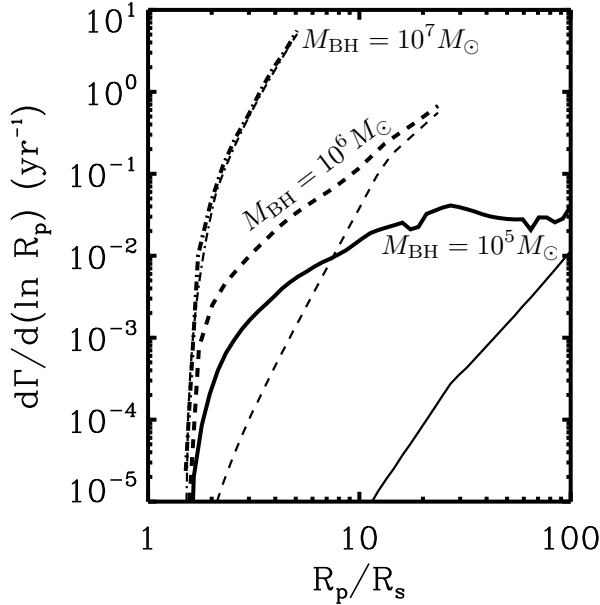


Figure 10. Predicted detection rates as a function of pericenter distance R_p/R_S for the Pan-STARRS 3π survey at g -band (see Table 1). Results are shown for $M_{\text{BH}} = 10^5 M_\odot$ (solid), $10^6 M_\odot$ (dashed), and $10^7 M_\odot$ (dot-dashed), assuming a non-rotating BH. The thin/light lines are for the disk emission alone, while the thick/heavy lines include the emission from both the disk and the photoionized unbound material. The photoionized material significantly increases the rates for low M_{BH} and small R_p/R_S . These rates do not include emission from super-Eddington outflows at early times; those results are shown in Figs. 12 & 13. The small fluctuations in the results for $M_{\text{BH}} = 10^5 M_\odot$ are due to difficulties in performing Cloudy calculations at very high densities.

bound material to return to pericenter ($t_{\text{outflow}} \sim t_{\text{fallback}}$; eq. [1]); for $R_p = R_T$, the transition from t_{edge} to t_{fallback} occurs at a somewhat lower BH mass of $M_{\text{BH}} \lesssim 4 \times 10^5 M_\odot$. Figure 11 shows that most flares last longer than the few-day cadences of surveys like PTF, Pan-STARRS MDS, and LSST, but are much shorter than the months-long cadence of the Pan-STARRS 3π survey. ROSAT and GALEX are unlikely to have detected events during this phase due to insufficient cadence and sky coverage.

In Figure 12, we plot detection rates as a function of R_p/R_S for $M_{\text{BH}} = 10^5 M_\odot$, $10^6 M_\odot$, and $10^7 M_\odot$, all for the Pan-STARRS 3π survey at g -band. At small R_p/R_S , the edge of the outflow limits the size of the photosphere. As R_p/R_S increases, the radius of the photosphere at t_{edge} increases and so the rates increase. For $M_{\text{BH}} = 10^6 M_\odot$ and $10^7 M_\odot$ at the largest R_p/R_S , the photosphere is no longer limited by the edge of the outflow, and the maximum luminosity occurs at t_{fallback} . For large R_p/R_S , the rate declines as the photosphere recedes inward.

In Figure 13, we plot overall detection rates at g -band for Pan-STARRS 3π and MDS, PTF, and LSST. In the left-most panel, we assume that 10% of the falling back material flows out in the wind ($f_{\text{out}} = 0.1$), as we have previously. Here we restrict detections to redshifts $z < 1$, where our assumed tidal disruption rate per galaxy is appropriate. The

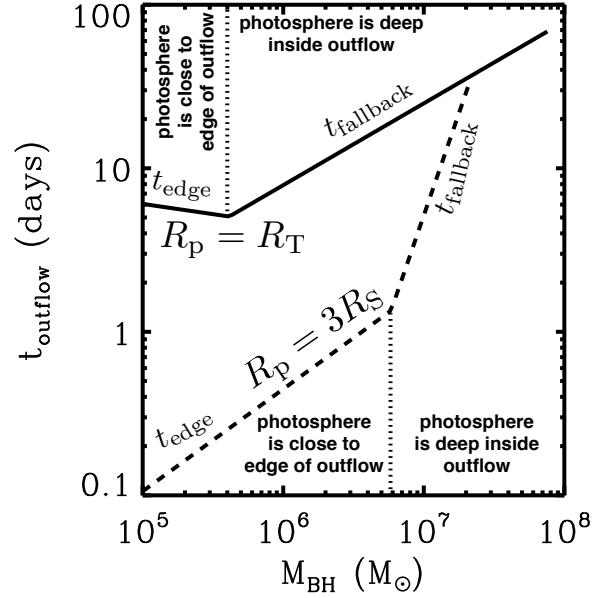


Figure 11. Duration of peak luminosity during the early super-Eddington outflow phase, as a function of M_{BH} for $R_p = 3R_S$ and $R_p = R_T$ (for $f_{\text{out}} = 0.1$ and $f_v = 1$; see eqs. [5] & [6]). The vertical dotted lines mark the boundary between events where the edge of the outflow limits the size of the photosphere (lower BH masses) and where it does not (higher BH masses). The flares from super-Eddington outflows typically last longer than the few-day cadence of surveys like PTF, Pan-STARRS MDS, and LSST, but they are often short enough that they would not be detected in surveys optimized solely for supernovae.

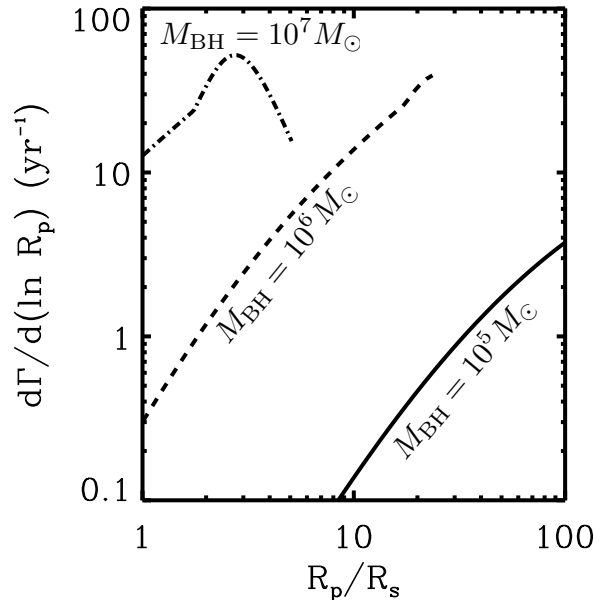


Figure 12. Predicted detection rates for emission from super-Eddington outflows at early times (for $f_{\text{out}} = 0.1$ and $f_v = 1$; see eqs. [5] & [6]). Results are shown as a function of R_p/R_S for $M_{\text{BH}} = 10^5 M_\odot$, $10^6 M_\odot$, and $10^7 M_\odot$, all for a Pan-STARRS 3π -like survey at g -band (see Table 1).

Pan-STARRS 3π survey should detect 200 yr^{-1} , while the MDS should detect 20 yr^{-1} because of its smaller spatial volume. PTF should detect 300 yr^{-1} as well, since its fast cadence makes up for its smaller spatial volume relative to the Pan-STARRS 3π survey. LSST’s large spatial volume and rapid cadence should allow it to detect 6000 yr^{-1} ! Assuming the survey parameters and strategy described in §5.1 and Table 1, SASIR should detect $\sim 100\text{ yr}^{-1}$ as well.

In the central panel of Figure 13, we plot detection rates for redshifts $z > 1$ to highlight the possibility of studying tidal disruption events at cosmological distances. Deep surveys like MDS will be sensitive to events far beyond $z \sim 1$. Even the shallower 3π survey could detect ~ 30 events per year at $z > 1$. Our predicted rates at $z > 1$ are particularly uncertain: higher redshift sources are more likely to be obscured, and the lower mass BHs of interest for tidal disruption are still growing significantly in mass at these redshifts (Heckman et al. 2004) so the tidal disruption rate and mass function become less certain. Nonetheless, the fact that tidal disruption flares will be detectable at $z > 1$ with forthcoming surveys highlights that these sources may become a strong probe of the evolution of $\sim 10^6 - 10^8 M_\odot$ BHs.

In the rightmost panel of Figure 13, we show the sensitivity of our predictions to uncertainty in the outflow model by plotting the rates for the Pan-STARRS 3π survey for different assumptions about the fraction of the material that is blown away in the outflow, f_{out} . For $f_{\text{out}} \sim 0.3$, the detection rate is 600 yr^{-1} , while for $f_{\text{out}} \sim 0.01$ it falls to 8 yr^{-1} . The rate falls rapidly at the highest M_{BH} because the outflow is optically thin. Figure 13 shows that even if we very conservatively assume that only 1% of the material is blown away when the fallback rate is super-Eddington, upcoming optical surveys like Pan-STARRS should still be able to detect a significant number of tidal disruptions during the super-Eddington phase.

6 DISCUSSION

We have calculated the spectra and light curves produced by the tidal disruption of a solar-type star by a massive black hole. Upcoming optical transient surveys should detect many such events (§5). Our results demonstrate that there are at least three different emission components that are important during tidal flares: (1) outflows at early times when the fallback rate is super-Eddington, (2) a compact ($\lesssim 10 - 100 R_s$) accretion disk around the BH, and (3) stellar debris that is unbound during the disruption and forms an outflowing “wedge” in the equatorial plane (see Fig. 1). It is also possible that the super-Eddington fallback powers a lower-density magnetically-dominated jet, but the properties of such a jet are difficult to predict so we do not consider this potential source of emission.

Each of these three components contributes to the total emission from tidal disruption flares. At early times, the super-Eddington outflows likely dominate, producing a few- to 10-day optical-infrared flare with a luminosity comparable to that of a supernova (Figs. 2-4 & 11). As the fallback rate decreases below the Eddington rate, these outflows will diminish, revealing the underlying accretion disk that emits primarily in the UV to soft X-rays (Fig. 5); at this time, the

optical emission is likely to be much less than that of a typical AGN—and well below that of the super-Eddington phase (Fig. 3)—because the accretion disk is not very spatially extended. The central UV and soft X-ray source photoionizes the inner edge of equatorial stellar debris, producing a spectrum of broad emission lines (Figs. 5, 6, & 7) whose “rest” wavelength should be either blueshifted or redshifted with respect to the host galaxy depending on the line of sight of the observer relative to the escaping material. We find that this spectroscopic signature of tidal flares is the strongest for low mass BHs because the equatorial stellar debris occupies the largest solid angle in these systems (eq. [25]).

Although the above stages are the focus of this paper, for completeness we briefly discuss the rest of the evolution of a tidal disruption event. As the fallback rate continues to decrease below the Eddington rate, the viscous time in the thin disk (eq. [21]) increases and becomes comparable to the time t since disruption; at this point, matter begins to build up rather than rapidly accreting onto the BH. For disruption at $R_p \sim R_T$, which is likely to produce a significant fraction of the events (Figs. 10 & 12), we estimate that this occurs $\sim 3\alpha_{0.1}^{3/7}$ years after disruption, when the fallback rate has decreased to $\dot{M}_{\text{fallback}} \sim 0.2\alpha_{0.1}^{-5/7} M_6^{-2/3} \dot{M}_{\text{Edd}}$ (where $\alpha \equiv 0.1\alpha_{0.1}$ is the dimensionless viscosity). Separately, we expect a significant change in the thermodynamics of the disk when $\dot{M}_{\text{fallback}} \simeq \alpha^2 \dot{M}_{\text{Edd}} \sim 10^{-2} \dot{M}_{\text{Edd}}$. Below this accretion rate, the material will no longer cool efficiently when it circularizes and shocks upon returning to pericenter. Instead of cooling to form a thin disk, the material will be shock heated to form a geometrically thick, radiatively inefficient accretion flow. In general, both geometrically thin/optically thick and geometrically thick/radiatively inefficient disks appear to be stable accretion solutions for a given $\dot{M} \lesssim 10^{-2} \dot{M}_{\text{Edd}}$. However, in this case, the boundary condition that matter shocks up to the virial temperature upon returning to pericenter picks out the radiatively inefficient solution once $\dot{M}_{\text{fallback}} \lesssim 10^{-2} \dot{M}_{\text{Edd}}$. Because the viscous time in a thick disk is $\sim \alpha^{-1}$ times the dynamical time, once the accretion becomes radiatively inefficient, the viscous time is always much shorter than the orbital period of matter returning to pericenter. Moreover, the transition to radiatively inefficient accretion happens at a time comparable to when matter would otherwise begin accumulating in a thin disk, particularly for more massive BHs. This suggests that there is typically only a limited range of accretion rates (and time) during which the “spreading disk” solution of Cannizzo et al. (1990) applies. Instead, at late times matter will rapidly accrete via a thick disk and the accretion rate will decay as $\sim \dot{M}_{\text{fallback}} \propto t^{-5/3}$. As in X-ray binaries (Remillard & McClintock 2006), we expect that the thermodynamic transition at $\sim 10^{-2} \dot{M}_{\text{Edd}}$ will be accompanied by a significant change in the luminosity and spectrum of the disk, and perhaps also by the production of relativistic jets. This should be explored in more detail in future work.

Having summarized our key results and the timeline of a tidal disruption event, we now discuss some uncertainties in our models, observational challenges to detecting tidal flares, and the astrophysical applications of studies of tidal disruption events.

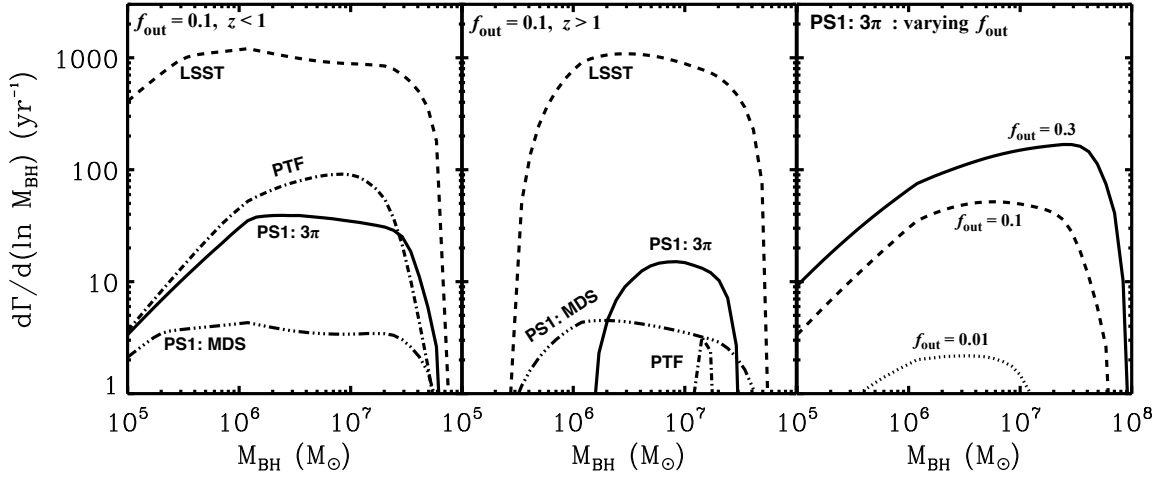


Figure 13. Predicted detection rates for emission at g -band from super-Eddington outflows for various optical transient surveys. In the leftmost panel, we use our standard outflow model in which $f_{\text{out}} = 0.1$ and $f_v = 1$ (see eqns [5] & [6]), and restrict detections to $z < 1$. In the central panel, we plot detection rates for $z > 1$ to illustrate the potential for surveys to be sensitive to the cosmological evolution of BHs; note that PTF is not deep enough to detect flares beyond $z \sim 1$. In the rightmost panel, we vary f_{out} from 0.3 to 0.01 to illustrate the sensitivity of our results to uncertainties in the outflow physics.

6.1 Super-Eddington Outflows

In §2.1, we described our simple model for outflows driven when the fallback rate is super-Eddington. Energy conservation implies that the falling back material initially remains bound after returning to pericenter and circularizing, but even small amounts of accretion can release additional energy and drive a powerful outflow. There is, however, a significant uncertainty in precisely how much of the falling back material is blown away, and in the kinematics of the outflow. We assume that the gas expands roughly spherically from the BH, but the flow is probably somewhat collimated along the pole, due to the original angular momentum of the stellar debris. Some photons can then leak out through the sides of the outflow rather than continuing to drive the expansion; in this case, the overall emission would be somewhat hotter and fainter, with a dependence on viewing angle.

We have parameterized the terminal velocity of the outflow using $v_{\text{wind}} = f_v v_{\text{esc}}(2R_p)$, and the mass outflow rate using $\dot{M}_{\text{out}} \equiv f_{\text{out}} \dot{M}_{\text{fallback}}$; in all of our calculations, we have assumed that $f_v \sim 1$. If the gas actually expands more slowly ($f_v < 1$), its density will be larger, so the photosphere will be larger, increasing the optical fluxes and detection rates. In the extreme case in which there is no unbound outflow, but super-Eddington fallback leads to a radiation-pressure-supported atmosphere around the BH that slowly expands until the photons can diffuse out, we also expect significant optical luminosities during the super-Eddington phase (e.g., Loeb & Ulmer 1997).

It is worth noting that our predictions for the radiation from super-Eddington outflows are particularly uncertain for low M_{BH} and small R_p/R_S , when the edge of the outflow limits the radius of the photosphere and determines both the peak luminosity (Fig. 3) and duration (Fig. 11) of the flare; this does not, however, significantly influence our total predicted rates (Fig. 12).

Figure 13 shows that even if the outflow rate is just

a few percent of the fallback rate ($f_{\text{out}} \sim 0.01 - 0.1$), the outflowing gas is sufficiently bright in the optical that forthcoming surveys should detect a significant number of tidal disruption flares. This makes early-time optical flares from the tidal disruption of stars an extremely promising candidate for current and future optical/infrared transient surveys. (We discuss some practical issues associated with detecting these sources in §6.3.) In this context, we note that in the radiation hydrodynamic simulations of accretion at $\dot{M} = 100\dot{M}_{\text{Edd}}$ carried out by Ohsuga et al. (2005), $\sim 10\%$ of the gas becomes unbound, $\sim 10\%$ accretes, and the remaining $\sim 80\%$ is marginally bound and may (or may not) eventually accrete as well. These precise values will depend on the pericenter of the star, with smaller R_p/R_S likely leading to smaller f_{out} , i.e., a smaller fraction of the gas being blown away. Future observational constraints on the luminosity, spectrum, and timescale of the super-Eddington outflow phase should be able to strongly constrain the value of f_{out} in individual events. These results will have important implications for how massive BHs grow. In particular, if f_{out} is typically modest, this would imply that black holes can accrete at rates far above the Eddington rate, perhaps helping to explain how supermassive BHs ($M_{\text{BH}} \gtrsim 10^8 M_\odot$) can be observable as luminous quasars as early as $z \sim 6$.

Figure 13 also demonstrates that deep optical surveys such as the Pan-STARRS MDS and LSST will be sensitive to tidal flares at high redshift. These surveys may thus provide a powerful probe of the BH mass function and stellar dynamics in galactic nuclei as a function of redshift. For example, at $z \sim 0.1$, BHs having $M_{\text{BH}} \lesssim 10^7 M_\odot$ are still growing significantly in mass (Heckman et al. 2004) and thus their disruption rates may evolve significantly with redshift. In addition, galaxy mergers, which are more common at $z \sim 1 - 2$, could substantially increase the tidal disruption rate: Chen et al. (2009) find rates of up to $\sim 1 \text{ yr}^{-1}$ for $\sim 10^5$ years after the merger due to three-body interactions between stars and a binary BH.

6.2 The Accretion Disk, Photoionized Gas, & Broad Emission Lines

We now consider several aspects of our model for the accretion disk, broad emission lines, and the material unbound during the disruption (§§2.2 and 3). Our accretion disk model is designed to describe the emission from the time when the disk first forms through the following few years. During much of this period, the fallback rate is super-Eddington, and we expect the disk to be optically and geometrically thick, with radiation pressure dominating gas pressure. Once the fallback rate becomes sub-Eddington, the disk becomes geometrically thin and may be subject to viscous instabilities (although it is thermally stable; Hirose et al. 2009). These instabilities may lead to additional time dependence not captured in our models, particularly at late times when the viscous time in the thin disk becomes comparable to the orbital period of the material falling back to pericenter. As described above, once $\dot{M}_{\text{fallback}} \lesssim \alpha^2 \dot{M}_{\text{Edd}}$, the density is sufficiently low that the flow becomes radiatively inefficient and our model is no longer appropriate. The disk will then heat up and its spectrum will become significantly harder. This phase may be detectable by hard X-ray transient surveys like EXIST.

It is also unclear how much tidal forces will spin up the rotation of the star as it approaches pericenter. We have assumed that the star is maximally spun up, so that stellar debris is accelerated to relative velocities $\Delta v \sim v_p (R_*/R_p)^{1/2}$ in the azimuthal direction. If in fact the spin-up is less effective, the onset of the flare, which occurs at the fallback time (eq. [1]), will be later by a factor of few and the solid angle subtended by the unbound equatorial debris will be somewhat smaller. This will not change our qualitative conclusions, only some of our quantitative results.

It is important to stress that the line emission we predict may well be an underestimate in all cases: the accretion disk will also photoionize the *back edge* of the material that was blown away during the super-Eddington phase, which is far from the BH once the outflows subside. Simple estimates indicate that the density and velocity of this outflowing gas are similar to that of the gas unbound at the time of disruption; as a result, irradiation of this gas will produce additional broad hydrogen lines. The equivalent width of these lines depends on the solid angle subtended by the super-Eddington winds, which, although uncertain, is likely to be significant. These lines are unlikely to depend as sensitively on M_{BH} and R_p/R_S as the emission lines from the equatorial debris (see Fig. 6 for the latter). As a result, observations of the line emission will help constrain the geometry of the outflowing gas created during the tidal disruption event.

In addition to emission lines from the back edge of the outflowing gas at late times, the photosphere of the super-Eddington outflow may at early times show strong *absorption lines*, particularly in the ultraviolet (much like the photosphere of a star); these lines would likely be highly blueshifted relative to the lines of the host galaxy. Finally, we reiterate that we expect very little narrow forbidden line emission from tidal disruption events: the outflowing stellar debris is too dense to produce forbidden lines, and there is insufficient time to photoionize ambient lower density gas far from the BH. It is possible that there is ambient gas in the galactic nucleus sufficiently close to the BH to produce

forbidden lines on a $\lesssim 1$ yr timescale, but the prevalence of such gas is currently poorly understood.

6.3 Observational Considerations

Candidate detections of tidal disruption flares have thus far been selected by their UV and soft X-ray emission (predominantly via GALEX, ROSAT and XMM-Newton). The emission at these wavelengths is primarily produced by the accretion disk, which is brighter for larger M_{BH} . As a result, these surveys are most sensitive to BHs having $M_{\text{BH}} \sim 10^7 - 10^8 M_\odot$. UV and X-ray selected events are likely to be discovered somewhat after the initial period of super-Eddington fallback, because the outflow during that phase probably precludes direct observation of the underlying accretion disk from many viewing angles. This outflowing material could also be a significant source of obscuration even at late times when the fallback rate is sub-Eddington.

The accretion disk emission we predict for UV-selected events is broadly consistent with the GALEX candidates: UV luminosities of $\sim \text{few} \times 10^{43} \text{ erg s}^{-1}$, optical luminosities of $\sim \text{few} \times 10^{41} \text{ erg s}^{-1}$, blackbody temperatures of $T \sim \text{few} \times 10^4 - \text{few} \times 10^5 \text{ K}$, and bolometric luminosities of $L_{\text{bol}} \sim 10^{45} \text{ erg s}^{-1}$. The events selected from soft X-rays have less data, but typically have soft X-ray luminosities of $\sim 10^{43} - 10^{44} \text{ erg s}^{-1}$. This emission may be from the accretion disk, at energies just above the blackbody peak, or may be from an X-ray power-law tail with 1 – 10% of the bolometric luminosity. In addition, as discussed in §5.2, our model is consistent with ROSAT and GALEX rate estimates, provided that the tidal disruption rate per galaxy for BHs with $M_{\text{BH}} \sim 10^7 M_\odot - 10^8 M_\odot$ is $\gamma \sim 10^{-5} \text{ yr}^{-1}$. This constraint already suggests that galactic nuclei in the nearby universe are relatively spherical, rather than triaxial, because the expected disruption rate is significantly higher in the latter case (Merritt & Poon 2004).

As described in §4, the spectral signature of the equatorial stellar debris is a transient spectrum of broad emission lines shifted in wavelength relative to the host galaxy. We do not expect forbidden lines (e.g. [NII], [SII], [OI], [OIII]) to be present, because the density in the unbound material is too high.⁷ For several reasons, it is not surprising that this spectral signature has yet to be seen. First, the tidal flare candidates are likely from relatively high-mass BHs; in those events, the unbound stellar debris subtends a small solid angle (eq. [25]) and so the emission lines should be $\lesssim 1\%$ of the bulge luminosity. Future optically-selected tidal flares are more likely to show detectable lines. It is also important to note that most standard searches for AGN in optical/infrared surveys use forbidden lines to identify nuclear activity, and have not specifically looked for faint, broad lines offset from the host galaxy's lines. Tidal disruption events may yet be hiding in archival spectroscopic data.

We predict that outflows during the super-Eddington fallback phase have peak optical luminosities of $\sim 10^{43} - 10^{44} \text{ erg s}^{-1}$ and characteristic decay timescales of ~ 10 days

⁷ The 5007 Å line of [OIII] does appear at late times for the lowest M_{BH} and R_p , where the densities fall below this ion's critical density after about a year.

(Figs. 4 & 11). These events are sufficiently bright that a natural concern is whether our predictions can already be ruled out by optical supernova searches such as the Supernova Legacy Survey and Stripe 82 in the Sloan Digital Sky Survey. Although a careful search of archival data is clearly warranted, we do not believe that current observations are necessarily that constraining, for two reasons. First, the outflow phase can be relatively brief and many survey cadences may be insufficient to find these events. Most importantly, however, tidal flares could be readily mistaken for AGN and thus discarded. Indeed, most supernova searches discard galactic nuclei in order to avoid confusion with AGN and optimize their probability of detecting supernovae.

Optically detecting a tidal flare may require disentangling the flare emission from that of the BH's host galaxy. For example, at a distance of 300 Mpc, a ground-based optical survey with a resolution $\sim 1''$ should just be able to resolve a kiloparsec-sized bulge. Bulges are found to be ~ 700 times more massive than their central BHs (Haring & Rix 2004). Super-Eddington outflows typically shine at $10^{43} - 10^{44} \text{ erg s}^{-1}$ (see Fig. 4), so this phase should be at least as bright as the host galaxy and readily detectable given sufficient attention to sources in galactic nuclei and careful screening to rule out an unsteady AGN. By contrast, the typical optical luminosity of the accretion disk itself is $10^{40} - \text{few} \times 10^{41} \text{ erg s}^{-1}$ (see Fig. 3). The accretion disk would thus brighten the host bulge by only a few percent. Photometric detections of late-time flares will require very careful bulge subtraction. As a result, shallow, wide-area surveys such as PTF are more likely to find the late-time disk emission than narrow deep surveys such as the Pan-STARRS MDS. As an additional complication to finding tidal flares, optical extinction in galactic nuclei can be significant (although less than at UV or soft X-rays); as a result, some fraction of optical tidal flares may not be detectable due to obscuration. Infrared surveys such as SASIR, which are also very sensitive to tidal disruption events (Table 1), will be particularly immune to the effects of obscuration.

Type II supernovae in the nuclear regions of galaxies may be confused with tidal disruption events, as both have quite blue colors. For sources at ~ 300 Mpc, we estimate that such supernovae will occur within $\sim 1''$ of the galactic nucleus at a rate of $\sim 10^{-4} \text{ yr}^{-1}$, perhaps an order of magnitude more often than tidal disruption events; at higher redshift the contamination from supernovae will be more significant, but follow-up imaging at high spatial resolution and/or spectroscopic follow-up should help classify these events and distinguish tidal flares from nuclear supernovae.

6.4 Astrophysical Applications

Theoretical calculations of the tidal disruption rate per galaxy, γ , vary substantially and can have complicated dependences on BH mass and pericenter distance (e.g., Magorrian & Tremaine 1999). The rate model we implement is consistent with theoretical estimates and is sufficiently simple that the reader can easily scale our results to different model parameters (eq. [32]). We have assumed that the rate at which stars enter the disruption zone ($R_S < R_p < R_T$) is independent of BH mass, and constant with $\ln R_p$. A star may venture deep into the disruption zone ($R_p \sim R_S$) on its last orbit if its change in angular momentum over one

dynamical time is large enough—at least of order the maximum angular momentum for disruption. This condition is satisfied in the full loss cone regime, and marginally satisfied in the outskirts of the diffusive regime. For realistic stellar density profiles, the disruption rate is dominated by the boundary between these two regimes (e.g., Alexander 2005), so many stars probably do take large enough angular momentum steps to arrive at $R_p \ll R_T$. In the diffusive regime, the disruption rate per $\ln R_p$ varies weakly with $\ln R_p$, consistent with our assumption in §5. Given the sensitivity of the optical-infrared emission from tidal flares to R_p , upcoming surveys should significantly improve our knowledge of the stellar dynamics in galactic nuclei.

Our results demonstrate that optical transient surveys will be quite sensitive to the lowest mass BHs in galactic nuclei, both because of the outflows produced when the fallback rate is super-Eddington and because of the large angle subtended by the equatorial stellar debris. Such BHs are otherwise difficult to detect because their host galaxies are faint, it is difficult to resolve their small spheres of influence, and even when they are active, their Eddington luminosities are low. The space density of $10^5 - 10^6 M_\odot$ BHs and the stellar density profiles in the galaxies they inhabit are only moderately well-constrained at present (e.g., Greene & Ho 2007), as is the role of tidal disruption in growing these BHs. Optical searches for tidal flares should thus prove to be a powerful probe of low-mass BHs and their host galaxies.

ACKNOWLEDGMENTS

We thank Josh Bloom, Phil Chang, Eugene Chiang, Luis Ho, and Enrico Ramirez-Ruiz for helpful discussions; we also thank Phil Hopkins for providing the black hole mass function in tabular form; and we thank Gary Ferland, Ryan Porter and Peter van Hoof at the Cloudy discussion board for rapid and helpful replies to our questions. LES and EQ are supported in part by the David & Lucile Packard Foundation and NASA Grant NNG06GI68G. LES dedicates this work to the memory of two shining stars, Sandra Strubbe and Doug Baker.

REFERENCES

- Abramowicz M.A., Czerny B., Lasota J.P., Szuszkiewicz E. 1988, *ApJ*, 332, 646
- Alexander T. 2005, *Physics Reports*, 419, 65
- Ayal S., Livio M., Piran, T. 2000, *ApJ*, 545, 772
- Blandford, R.D., Begelman M.C. 1999, *MNRAS*, 303, L1
- Bloom J.S., Prochaska J.X., Lee W. et al. 2009, arXiv:0905.1965v1 [astro-ph.IM]
- Bogdanović T., Eracleous M., Mahadevan S., Sigurdsson S., Laguna P. 2004, *ApJ*, 610, 707
- Brassart M., Luminet J.-P. 2008, *Å*, 481, 259
- Cannizzo J.K., Lee H.M., Goodman J. 1990, *ApJ*, 351, 38
- Chen X., Madau P., Sesana A., Liu, F.K. 2009, arXiv:0904.4481v1 [astro-ph.GA]
- Donley J.L., Brandt W.N., Eracleous M., Boller T. 2002, *ApJ*, 124, 1308
- Esquej P., Saxton R.D., Freyberg M.J., Read A.M., Altieri B., Sanchez-Portal M., Hasinger G. 2007, *A&A*, 462, L49

- Evans C., Kochanek C. 1989, ApJL, 346, L13
- Ferland G.J., Korista K.T., Verner D.A., Ferguson J.W., Kingdon J.B., Verner E.M. 1998, PASP, 110, 761
- Gezari S., Martin D.C., Milliard B. et al. 2006, ApJ, 653, L25
- Gezari S., Basa S., Martin D.C. et al. 2008, ApJ, 676, 944
- Gezari S., Heckman T., Cenko S.B. et al. 2009, arXiv:0904.1596v1 [astro-ph.CO]
- Greene J.E., Ho L.C. 2007, ApJ, 670, 92
- Grindlay J.E. 2004, AIP Conf. Proc., 714, 413
- Guillochon J., Ramirez-Ruiz E., Rosswog S., Kasen D. 2008, arXiv:0811.1370v2 [astro-ph]
- Haring N., Rix H.W. 2004, ApJ, 604, L89
- Heckman T.M., Kauffmann G., Brinchmann J., Charlot S., Tremonti C., White S.D.M. 2004, ApJ, 613, 109
- Hirose S., Krolik J., Blaes O. 2009, ApJ, 691, 16
- Hopkins P.F., Richards, G.T., Hernquist, L. 2007, ApJ, 654, 731
- Khokhlov A., Melia F. 1996, ApJL, 457, L61
- Kochanek C.S. 1994, ApJ, 422, 508
- Komossa S. 2002, Rev. Mod. Astron., 15, 27
- Koratkar A., Blaes O. 1999, PASP, 111, 1
- Lacy J.H., Townes C.H., Hollenbach D.J. 1982, ApJ, 262, 120
- Li L., Narayan R., Menou K. 2002, ApJ, 576, 753
- Lodato G., King A.R., Pringle J.E. 2009, MNRAS, 392, 332
- Loeb A., Ulmer A. 1997, ApJ, 489, 573
- Magnier E. 2007, ASPC, 364, 153, ed. C. Sterken (San Francisco: ASP)
- Magorrian J., Tremaine S. 1999, MNRAS, 309, 447
- Merritt D., Poon M.Y. 2004, ApJ, 606, 788
- Ohsuga K., Mori M., Nakamoto T., Mineshige S. 2005, ApJ, 628, 368
- Perets H.B., Hopman C., Alexander T. 2007, ApJ, 656, 709
- Phinney E.S. 1989, in IAU Symp. 136, The Galactic Center, ed. M. Morris (Dordrecht: Kluwer)
- Ramirez-Ruiz E., Rosswog S. 2009, ApJL, 697, L77
- Rau A., Kulkarni S.R., Law N.M. et al. 2009, arXiv:0906.5355v1 [astro-ph.CO]
- Rauch K.P., Tremaine S. 1996, NewA, 1, 149
- Rees, M. 1988, Nature, 333, 523
- Remillard R., McClintock J. 2006, ARA&A, 44
- Rossi E.M., Begelman M.C. 2009, MNRAS, 392, 1451
- Rybicki G.B., Lightman A.P. 1979, Radiative Processes in Astrophysics (New York: John Wiley & Sons, Inc.)
- Shakura N.I., Sunyaev R.A. 1973, A&A, 24, 337
- Ulmer A. 1999, ApJ, 514, 180
- Zhao H., Haehnelt M.G., Rees, M.J. 2002, NewA, 7, 385